Quaternary Science Reviews 260 (2021) 106915

Contents lists available at ScienceDirect

Quaternary Science Reviews

journal homepage: www.elsevier.com/locate/quascirev

Invited paper

Neodymium isotope evidence for coupled Southern Ocean circulation and Antarctic climate throughout the last 118,000 years

Thomas John Williams [a, *], Ellen E. Martin [a], Elisabeth Sikes [b], Aidan Starr [c], Natalie E. Umling [d], Ryan Glaubke [b]

[a] Department of Geological Sciences, University of Florida, Gainesville, Fl, USA
[b] Department of Marine and Coastal Sciences, Rutgers University, New Brunswick, NJ, USA
[c] School of Earth and Environmental Sciences, Cardiff University, Cardiff, Wales, UK
[d] Department of Earth and Planetary Sciences, American Museum of Natural History, New York, NY, USA

ARTICLE INFO

Article history:
Received 30 October 2020
Received in revised form
23 March 2021
Accepted 23 March 2021
Available online xxx

Handling Editor: A. Voelker

Keywords:
Paleocirculation
Paleoclimate
Southern Ocean
Neodymium isotopes
Sortable Silt
Antarctic Climate
Ocean Circulation

ABSTRACT

The chain of events surrounding the initiation and intensification of the last glacial cycle remain relatively poorly understood. In particular, the role of Southern Ocean paleocirculation changes is poorly constrained, in part, owing to a paucity of sedimentary records from this region. In this study we present multiproxy data – including neodymium isotope and sortable silt measurements – for paleocirculation changes within the deep (3167 m water depth) Indian sector of the Southern Ocean from a new sediment core, TT1811-34GGC (41.718°S, 80.163°E). We find a tight coupling between circulation changes, Antarctic climate, and atmospheric CO_2 concentrations throughout the last 118,000 years, even during the initial stages of glacial inception of Marine Isotope Stage (MIS) 5.4 to 5.1. We find that periods of cooling correspond to reductions in the entrainment of North Atlantic-sourced waters within the deep Southern Ocean, as evidenced by more radiogenic neodymium isotope values of deep water bathing our core site. Cooling also corresponds to generally slower bottom water flow speeds, as indicated by finer sortable silt size fractions. A reduction in entrainment of North-Atlantic sourced waters occurred during MIS 5.4–5.1, when Atlantic circulation was strong, suggesting a Southern hemisphere control on paleocirculation changes at that time. We hypothesise that expanded Southern Ocean sea-ice during MIS 5.4 increased the density of the deep Southern Ocean, reducing the ability of Atlantic-sourced waters to mix into Lower Circumpolar Deep Water. This led to an expanded contribution of Pacific Deep Water within the lower circulation cell and increased stratification within the deep Southern Ocean. These paleocirculation changes can help account for the reduction in atmospheric CO_2 across the MIS 5.5 to 5.4 transition, and in doing so help explain the chain of events surrounding the decent into the last glacial period.

1. Introduction

1.1. The last glacial cycle

The last period of major global climatic change, the transition from cold glacial to warm interglacial conditions that occurred approximately 20,000–11,000 years ago, has long been the focus of intense investigation in the paleoclimate community (e.g. Shakun et al., 2012; Sigman et al., 2010; Lynch-stieglitz et al., 2007). Just prior to this interval, during the Last Glacial Maximum (LGM, 22–18 ka), atmospheric CO_2 levels were approximately 80 ppm lower (e.g Monnin et al., 2001), global temperatures were between 3.5 and 6.5° colder (Shakun et al., 2012; Snyder 2016; Tierney et al., 2020), and the expansion of continental ice resulted in global sea level that was as much as 125–134 m lower, than the late Holocene (0–14 ka; Lambeck et al., 2014; Yokoyama et al., 2018). It is widely accepted that the magnitude of cooling and continental ice expansion at the LGM was amplified by the reduction in atmospheric CO_2 (e.g. Shakun et al., 2012; Marcott et al., 2014), and that more CO_2 was sequestered within the ocean at that time than is the case today (Yu et al., 2020; Curry and Oppo, 2005; Gebbie et al., 2015).

Debate surrounding these climatic changes has primarily focused on the mechanisms that explain the rapid shift from a set of

* Corresponding author.
E-mail addresses: thomas.williams@ufl.edu, tom.jw88@gmail.com (T.J. Williams).

https://doi.org/10.1016/j.quascirev.2021.106915
0277-3791/

initial boundary conditions at the LGM, i.e. large northern hemisphere ice sheets, low atmospheric CO_2 concentrations, and reconfigured oceanic and atmospheric circulation, through millennial-scale variations into the Holocene. The exact triggers that lead to abrupt warming during the last deglaciation are uncertain. However, numerous studies have identified changes in ocean circulation as a critical component in the transition from full glacial to full interglacial conditions, in particular the release of remineralised organic carbon from the ocean interior to the atmosphere (e.g. Curry and Oppo 2005; Sikes et al., 2017; Anderson et al., 2009; Martínez-Botí et al., 2015).

1.2. Initiation of the last glacial cycle

The mechanisms explaining how the planet descends into an ice age are even more uncertain than the triggers that cause deglaciations. Thus, an important corollary question to the drivers of deglaciation is the longer, more gradual changes that initiated the transition from the peak of the last interglacial period, approximately 129–123 ka, into the LGM (Kohfeld and Chase, 2017; Koutavas, 2018; O'Neill et al., 2019). However, there remains a paucity of high-resolution terrestrial and marine records spanning this interval compared with the most recent deglacial and Holocene (Oliver et al., 2010). Furthermore, modelling the long and often nuanced shifts in Earth's climate system leading into the LGM is difficult and computationally expensive (O'Neill et al., 2019). As such, the chain of events surrounding the onset of glaciation across the last interglacial period (MIS 5.5) to MIS 4, between 129 and 71 ka, remain uncertain. The initial stages of glacial inception, during MIS 5.4 to 5.1, are particularly poorly understood.

The first steps towards glacial conditions during the last glacial cycle occurred across MIS 5.5 to 5.4. This period encompasses the first major atmospheric CO_2 decline, with a decrease of ~25–30 ppm, most of which occurred rapidly between 115 and 108 ka (EPICA Community Members, 2004). This reduction in atmospheric CO_2 occurred amid a backdrop of a ~2 °C cooling in global sea surface temperatures, that fell from approximately 21.5°–19.5° across 123–110 ka, with cooling more severe at high latitudes (Kohfeld and Chase, 2017). Cooling recorded in Antarctic ice cores at this time began at 118 ka, approximately 3 kyr before the first drop in CO_2 which occurred around 115 ka (EPICA Community Members, 2004; EPICA Community Members, 2006). Antarctic cooling occurred in tandem with reduced summer insolation at 65°N, which reached its lowest value of the last glacial cycle at 114 ka. This decline in Northern Hemisphere insolation led to cooling of the North Atlantic region, cooling surface waters which went on to form Northern Component Water (NCW – used here to signify the ancient counterpart of North Atlantic Deep Water, NADW). NCW transmitted this cooling signal through the deep Atlantic Ocean and into the Southern Ocean, where NCW mixed with circumpolar waters (Koutavas, 2018). Upwelling of these circumpolar waters along the Antarctic continental margin ultimately allowed for the propagation of the cooling signal from the North Atlantic to surface waters in the high latitude Southern Ocean.

Global temperatures failed to recover following the northern hemisphere insolation minimum at 114 ka, with declining atmospheric CO_2 and expansion of continental ice across MIS 5.5 to 5.4 maintaining lower global temperatures (Kohfeld and Chase, 2017). Therefore, mechanisms to explain the initiation of the last glacial cycle must account for the timing and magnitude of the drop in atmospheric CO_2 of approximately 25–30 ppmv across the MIS 5.5 to MIS 5.4 transition. The CO_2 decrease at 115–108 ka cannot be attributed to biological productivity stimulated by increased iron export to the ocean, as it occurred prior to the first observed increases in southern hemisphere dust flux at 104 ka (Lambert et al., 2008). The combined oceanic effects of lower SST and increased salinity due to expanded continental ice during MIS 5.4 is estimated to explain a decrease in atmospheric CO_2 of only 13 ppmv, that would have been largely offset by a retraction of the terrestrial biosphere (Kohfeld and Chase, 2017; Ciais et al., 2012). To date, there is little proxy evidence for changes in deep ocean circulation during these initial stages of glaciation. However, recent modelling work invokes a weakening of overturning circulation and a corresponding increase in the storage of remineralised carbon within the deep Southern, Indian and Pacific oceans to explain this atmospheric CO_2 decline (O'Niell et al., 2019). Importantly, this model result suggests no change occurred in Atlantic Meridional Overturning Circulation (AMOC) at this time. The current lack of proxy evidence for deep circulation changes may therefore stem from the availability of sediment cores spanning this time period, which are predominantly located within the Atlantic basin (Oliver et al., 2010).

2. Background

2.1. The Southern Ocean and global climate

Global overturning circulation plays a central role in our climate system through regulation of the global heat budget and by influencing the size and distribution of the oceanic carbon reservoir. Conceptually, modern overturning circulation is often likened to two interconnected cells (Sloyan and Rintoul, 2001; Lumpkin and Speer 2007; Ferrari et al., 2014). Within the Atlantic basin northward flowing surface, thermocline and intermediate waters make up the upper circulation cell, while NADW, made up of precursor water masses formed in the Labrador, Greenlandic and Norwegian seas, flows southward through the Atlantic basin into the Southern Ocean. The majority of NADW flows into the Southern Ocean as Lower Circumpolar Deep Water (LCDW) where it upwells, loses buoyancy, and contributes to the formation of Antarctic Bottom Water (AABW). Some of this AABW returns to the deep Atlantic basin, where diapycnal mixing with NADW eventually returns it to the Southern Ocean. The rest of this AABW flows – along with LCDW and modified NADW – into the deep Indian and Pacific basins, making up the lower circulation cells within these basins. Diffuse mixing between these deep circumpolar waters and less dense Antarctic Intermediate Water (AAIW) create Indian (IDW) and Pacific Deep Water (PDW) within the respective ocean basins, which return to the Southern Ocean to form Upper Circumpolar Deep Water (UCDW). An important point is that wind-drive upwelling of UCDW within the Southern Ocean occurs north of upwelling LCDW. Upwelled UCDW flows north across the surface of the Southern Ocean, loses buoyancy and sinks to form AAIW and Subantarctic Mode Water (SAMW). These intermediate and mode waters, along with surface and thermocline waters, feed the upper circulation cell, completing the two-cell circulation. These two circulation cells are connected via upwelling and mixing within the Southern Ocean, and diffuse diapycnal mixing within the Atlantic, Indian and Pacific basins (Talley 2013). A key facet of this two-cell model of overturning circulation is that NADW flowing into the Southern Ocean is denser than IDW and PDW. NADW therefore sinks below PDW and IDW within the Southern Ocean to form LCDW, which supplies the precursor water masses to AABW. In this way, transformed NADW ultimately feeds both LCDW and AABW, and thus the lower circulation cell of the global oceans (Sloyan and Rintoul, 2001; Lumpkin and Speer 2007; Talley 2013).

Changes in the distribution, mixing proportions and carbon contents of the different water masses making up these global circulation cells – especially the lower cell – are thought to have been important in forcing and modulating past climatic change,

particularly on glacial-interglacial timescales (Curry and Oppo, 2005; McCave et al. 2008; Kohfeld and Ridgwell, 2009; Sikes et al., 2017). The Southern Ocean plays a uniquely critical role in the creation, advection, mixing and upwelling of water masses of both the upper and lower circulation cells. As such, the Southern Ocean is at the heart of many hypothesis for past climatic change (e.g. Knox and McElroy, 1984; Sarmiento and Toggweiler, 1984; Stephens and Keeling, 2000; Martin, 1990; Toggweiler et al., 2006; Anderson et al., 2009). Many of the mechanisms by which deep ocean circulation can impact global climate invoke increases in the carbon inventory of the lower circulation cell, ultimately at the expense of atmospheric CO_2 concentrations. These mechanisms include: reduced mixing between − and wind-driven upwelling of − deep water masses, leading to a stratification of the ocean interior and reduced carbon exchange between the deep ocean and the atmosphere (Anderson et al., 2009; Ferrari et al., 2014); expansion of a carbon-rich, poorly ventilated AABW at the expense of carbon-poor, better ventilated North-Atlantic sourced waters (Curry and Oppo 2005; Skinner 2009; Sikes et al., 2000); a more sluggish overturning circulation, leading to a build-up of remineralised carbon within the deep oceans (Ballarotta et al., 2014); and a reduced capacity of upwelled deep water to outgas CO_2 into the atmosphere, either via increased sea-ice or a fresh-water stratification of the surface ocean (Stephens and Keeling, 2000).

Advection and mixing between circumpolar water masses within the Southern Ocean occurs largely within the clockwise flowing Antarctic Circumpolar Current (ACC). The ACC is the largest and longest oceanic current in the world, and is the only route directly connecting the Atlantic, Indian and Pacific basins. Reconstructing the mixing and circulation history of the circumpolar water masses that make up the upper and lower cells of global overturning circulation is key to understanding how ocean circulation has both forced and responded to changes in Earth's climate in the past. In this study, we present reconstructions of physical ocean circulation using neodymium isotopes and Sortable Silt ($\overline{ss}$) records located within the deep Indian sector of the Southern Ocean. We use these data to examine the role ocean circulation played in the initiation, intensification, and eventual end of the last glacial cycle, from MIS 5.5 to the Holocene.

2.2. Modern setting and neodymium isotope variability within the Southern Ocean

Seawater neodymium isotope ratios (ε_{Nd}, representing the deviation in parts per 10,000 of $^{143}Nd/^{144}Nd$ from the chondritic uniform reservoir) are a proxy that is widely applied to reconstruct past ocean circulation patterns. Different water masses within the modern ocean possess unique ε_{Nd} signatures, allowing us to trace flow path and mixing proportions between these waters (van de Flierdt et al., 2016; Tachikawa et al., 2017). The ε_{Nd} of water masses is imparted largely via seawater-sediment interactions along continental margins and the addition of dissolved and particulate Nd via riverine and aeolian inputs in regions of deep water formation. The end-member ε_{Nd} value of a given water mass is therefore a function of the continental geology surrounding the region of deep water formation, whereas within the ocean interior ε_{Nd} is determined largely by water mass mixing (Tachikawa et al., 2017). The old continental crust of the Canadian Shield imparts a highly unradiogenic (i.e. negative) ε_{Nd} signature on NADW (ε_{Nd} = approximately −13.5; Lambelet et al., 2016). This contrasts with the Pacific Ocean, where younger volcanic inputs impart a much more radiogenic (i.e. more positive) ε_{Nd} signature on PDW as it circulates through the Pacific basin (ε_{Nd} = approximately −2 to −4, van de Flierdt et al., 2016). Today, the ε_{Nd} composition of circumpolar water masses is controlled by mixing between inflowing NADW and PDW, with an additional relabeling of waters during AABW formation. The ε_{Nd} of modern AABW sourced in the Weddell Sea is approximately −8.8 (Stichel et al., 2012), while modern Ross Sea AABW is approximately −7.0 (Basak et al., 2015). The well-mixed nature of the ACC imparts a fairly uniform ε_{Nd} signature of c. −8 to −9 on modern CDW throughout much of the Southern Ocean (Piepgras and Wasserl, 1982 Science; Stichel et al., 2012; Basak et al., 2015). LCDW reaches values as unradiogenic as −10 off the southern tip of South Africa where modified NADW circulates into the Indian Ocean (Stichel et al., 2012). Within the Pacific sector of the Southern Ocean returning PDW imparts a more radiogenic signature of up to −6.4 on UCDW (Basak et al., 2015 station 44). However, this radiogenic Pacific signal rapidly diminishes as UCDW mixes with other circumpolar water masses (Tachikawa et al., 2017), resulting in ε_{Nd} of deep waters circulating through Drake Passage into the western Atlantic sector of the Southern Ocean of between −8.0 and −8.6 (Piepgras and Wasserl, 1982; Stichel et al., 2012).

2.3. ε_{Nd} reconstructions of Southern Ocean palaeocirculation

The past ε_{Nd} composition of LCDW flowing through Drake Passage is recorded by a series of coral samples located on the Sars Seamount, Interim Seamount and Shackleton Fracture Zone (Wilson et al., 2020). ε_{Nd} of seawater at abyssal depths within the Atlantic sector of the Southern Ocean is recorded in the composite record of cores RC11-83/TN057-21 (41°S, 4800 m water depth), located within the deep Cape Bain at the modern boundary of NADW and LCDW (Piotrowski et al., 2008, 2012). Ocean Drilling Project (ODP) Site 1088 (41.18°S, 2082 m. water depth) is today located just above the main inflow depth of NADW and is bathed in a mixture of NADW and UCDW (Hu et al., 2016). Site SK129-CR2 (3°N, 3800 m water depth) in the deep equatorial Indian Ocean is currently bathed in modified UCDW sourced within the Atlantic and Indian sectors of the Southern Ocean (Wilson et al., 2015). Where present, ε_{Nd} data from late Holocene sediments at each of these core sites is relatively homogenous and in good agreement with modern seawater values for CDW of c. −8 to −9 (Bertram and Elderfied, 1993; Stichel et al., 2012), reflecting the well mixed nature of the modern Southern Ocean. During the LGM, these ε_{Nd} records all demonstrate shifts towards more radiogenic ε_{Nd} values, indicative of a widespread reduction in NCW entering the Southern Ocean compared with the Holocene. There is also evidence for a shutdown in the export of AABW from the Weddell Sea region, which would further shift deep water ε_{Nd} towards more radiogenic values (Huang et al., 2020). This reduction in NCW is consistent with evidence from benthic foraminiferal $\delta^{13}C$ (McCorkle et al., 1998; Hodell et al., 2003; Lund et al., 2015; Curry and Oppo, 2005; Gebbie et al., 2015; Sikes et al., 2017), $\delta^{18}O$ (Sikes 2017), and Cd/Ca (Marchitto et al., 1998; Umling et al., 2019), reconstructed seawater carbonate ion concentrations (Yu et al., 2016, 2020) and south Atlantic and Southern Ocean sediment distributions during the LGM (Diekmann et al., 1999).

ε_{Nd} reconstructions from the deep (<3 km) SW Pacific and Pacific Southern Ocean also show shifts towards more radiogenic values of c. −5 during the LGM compared with c. −7.0 in the Holocene, again indicating reduced entrainment of NCW within the Southern Ocean (Noble et al., 2013; Hu et al., 2016). However, to date there are no reconstructions of past deep water ε_{Nd} from the Indian sector of the Southern Ocean owing to a paucity of sedimentary records from this region. There are also relatively few Southern Ocean ε_{Nd} records spanning the last glacial cycle (MIS 5.5–1) with which to examine the circulation configuration during glacial inception.

3. Methods

3.1. Study location

Core TT1811-34GGC (41.718°S, 80.163°E; 3167 m water depth) was retrieved east of the Kerguelen-Ile St Paul Island Passage, within the main flow path of the ACC (Fig. 1). This passage is located east of the main inflow of NADW into the Southern Ocean, which imparts LCDW with a relatively high salinity. Core TT1811-34GGC is today bathed in this high-salinity LCDW as it exits eastward through the Kerguelen-Ile St Paul Island Passage (Fig. 1). The major oceanic fronts within the Indian sector of the Southern Ocean are today steered northward via the bathymetric barrier imposed by the Kerguelen plateau. (Fig. 1). As the main flow path of the ACC follows these frontal zones, the ACC is therefore forced north of the Kerguelen Islands and through the bathymetric chokepoint of the Kerguelen-Ile St Paul Island Passage. Estimates of the total eastward flow through this passage are as high as 181 Sv (McCartney and Donohue, 2007), on the same order of magnitude as flow through Drake Passage. During the last glacial cycle, sea surface cooling and a northward shift in westerly winds shifted the major oceanic frontal zones of the Southern Ocean northward. As the ACC in our study region is bathymetrically constrained by the chokepoint of the Kerguelen-Ile St Paul Island Passage, core TT1811-34GGC is well placed to sample a significant volume of LCDW as it flows through the region even during periods of cooling during the last glacial cycle.

3.2. Sample preparation, bulk sedimentary $CaCO_3$, and isotopic analyses

Samples of 5 cc of sediment from core TT1811-34GGC were taken in 1 cm thick slices at 2–4 cm intervals throughout its 306 cm length for stable oxygen isotope, sortable silt and ε_{Nd} analyses. An additional subsample of 0.25 cc was taken from the same sample depths for measurements of bulk sedimentary $CaCO_3$ contents. Sediment samples were sieved at 63 μm and the <63 μm fraction was retained for sortable silt analyses. Benthic (*Cibicidoides kullenbergi*) and planktic (*Globigerina bulloides*) foraminifera were picked from the >150 μm and >250 μm fractions for stable oxygen isotope analyses at the University of Florida Light Stable Isotope Mass Spectrometry Laboratory in the Department of Geological Sciences. Measurements were performed on sample sizes of between 30 and 50 μg using a Kiel III carbonate preparation device coupled with a Finnigan-Mat 252 isotope ratio mass spectrometer. Results are presented as ‰ VPDB. Typical $\delta^{18}O$ precision of NBS-19

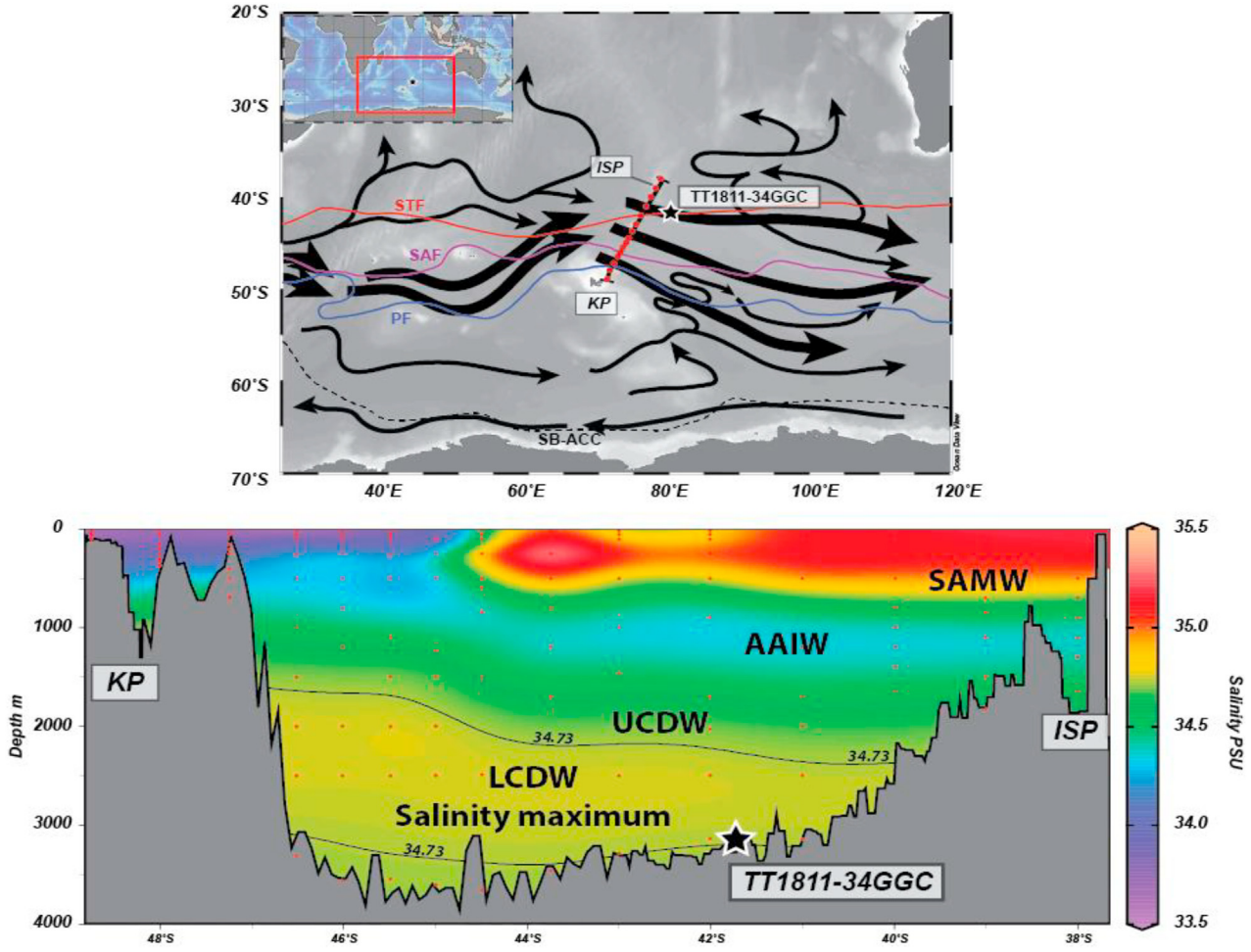

Fig. 1. A: Map of study area showing location of core TT1811-34GGC (black star). Black arrows show a schematic depiction of the main deep-water flow paths after McCartney and Donohue (2007) and Orsi et al.(1995), with thick arrows denoting the main body of flow within the ACC. The location of Ile St Paul (ISP) and the Kerguelen Plateau (KP) are highlighted, along with the average position of the Southern Boundary of the ACC (SB-ACC, black dashed), Polar Front (PF, blue), Subantarctic Front (SAF, purple) and Subtropical Front (STF, red) after Orsi et al., (1995). B: Hydrographic section showing salinity along hydrographic section MD91 (Park et al. 1991) across the Kerguelen-St Paul Island Passage. The 34.730 PSU contour is shown to highlight the high salinity core of LCDW.

standards was <0.01‰ VPDB.

The bulk sedimentary $CaCO_3$ content of samples was measured at the University of Florida at the Department of Geological Sciences. Total inorganic carbon was first measured coulometrically using a UIC 5017 CO_2 coulometer coupled with an AutoMate automated carbonate preparation device. Approximately 15 mg of sample was weighed into septum top tubes and placed into the AutoMate carousel. A double needle assembly was used to purge the sample vial of atmospheric gas using CO_2-free nitrogen carrier gas. Acid was then injected into the sample vial and evolved CO_2 was carried through a silver nitrate scrubber to the coulometer where total C as CO_2 is measured.

Between 150 and 200 mg of mixed species of planktic foraminifera were picked from the 150–250 μm fraction for analysis of neodymium isotopes, following the protocol outlined in Roberts et al. (2010). This protocol has been shown to faithfully extract seawater isotopic signatures (Tachikawa et al., 2014). Foraminifera tests were gently cracked open and clays removed before dissolution in 1 M acetic acid. REEs were isolated using Eichrom™ TRUspec resin and Nd was then extracted using Eichrom™ LNspec resin. All samples were measured for neodymium isotopes on the Nu Plasma ICP-Mass Spectrometer at the Department of Geological Sciences, University of Florida. Mass dependant fractionation during analyses was corrected for using an exponential correction to $^{146}Nd/^{144}Nd$ of 0.7219. Samples were bracketed by analysis of JNdi-1 standards corrected to 0.512115 (Tanaka et al., 2000). Quoted ε_{Nd} errors in this work are 2σ external error measured on the JNdi-1 standards, unless the internal error was greater, in which case reported errors are 2σ internal errors.

3.3. Sortable silt analyses

Sortable silt ($\overline{ss}$) samples were pre-treated following established methods (McCave et al., 1995) to remove biogenic carbonate and opal and then disaggregated in 0.2% sodium hexametaphosphate for at least 24 h on an end-over-end shaker. Measurements of silt size were made at Cardiff University on a Beckman Coulter Multisizer 4 with a 140 μm aperture, equipped with a Multisizer 4 Beaker with stirrer setting 35 to fully suspend the sediment. Between 2 and 4 aliquots of each sample were measured with each measurement making 70,000 counts in 256 size bins. Analytical precision was approximately + -0.3 μm and the average standard deviation between repeat measurements was 0.15 μm. The $\overline{ss}$ value reported is the average geometric mean grain size in the 10-63 μm range for at least 2 runs per sample.

3.4. Radiocarbon analyses

Radiocarbon measurements were made on planktic (*Globorotalia inflata*) samples from 8 depth intervals from core TT1811-34GGC (Fig. 3) at the University of California Irvine Keck-Carbon Cycle AMS facility (Table 1). These planktic ^{14}C ages were converted to calendar years B.P. using version 8.2 of the Calib software, utilizing the Marine20 calibration curve (Stuiver et al., 2020; Heaton et al., 2020). A regional reservoir offset (ΔR) of 442± 39 years was assigned, based on 14C analyses of pre-bomb mollusk shells from Kerguelen Islands (Paterne et al., 2019). Marine reservoir age estimates within the Southern Ocean can be difficult to constrain owing to variable air-sea gas exchange within sea-ice and upwelling of water masses introducing 'old' radiocarbon into surface waters. Reservoir ages are therefore likely to have changed in the past, especially during periods of increased sea ice coverage and changes in water mass circulation, such as the last glacial period and deglaciation. To assess the potential impact these effects may have had on our age model, we compared the age model using a constant ΔR, to one utilizing the time-varying offset in planktic-atmospheric radiocarbon ages observed by Gottschalk et al. (2020) in the independently dated sediments of nearby core MD12-3396CQ (−47.7°S, 86.7°E). The planktic-atmospheric 14C offsets of Gottschalk et al. (2020) were used to estimate the surface ocean radiocarbon offset from atmosphere at our core site, assuming that it was the same as at site MD12-339CQ. Planktic radiocarbon measurements at our core site were then corrected to atmospheric values using this offset, and calibrated using the IntCal20 calibration curve (Reimer et al., 2020). A comparison between the two age models shows good agreement between the two, with an average difference between the two of ~200 years over the last 26 ka. The maximum difference between the two age models, of ~600 calendar years, occurs during the mid-Holocene and Heinrich Stadial 1 (see SOM Fig. 1). This difference is on the same order as the estimated error in planktic-atmospheric offsets of Gottschalk et al. (2020), of ~500 years within the mid Holocene and ~700 years during Heinrich Stadial 1. However, the uncertainty associated with the planktic-atmospheric offsets of Gottschalk et al. (2020) increase to over 1000 years during the LGM. Due to this increase in uncertainty in planktic-atmospheric offset during the last glacial period, and the generally good agreement between the two age models, in this study we utilize the age model using the constant regional ΔR of Paterne et al. (2019).

Table 1
Radiocarbon ages of foraminifera shells (monospecific samples of *Globorotalia inflata*) from core TT1811-34GGC. Ages calibrated using Calib 8.1.0 using the Marine20 calibration curve (Heaton et al., 2020) assuming a local reservoir effect (ΔR) of 442 ± 39 years, from Paterne et al. (2019).

UCIAMS	Core Depth	14C age	1σ error	Age Range 2σ (yr BP)		Median Age
Code		(yr)	(yr)	Lower	Upper	(yr BP)
233843	0–1 cm	2535	20	2393	2739	2585
233844	20–21 cm	6930	20	7504	7809	7651
233845	24–25 cm	7155	25	7706	8015	7872
233846	32–33 cm	10,485	25	11,986	12,468	12,243
233847	48–49 cm	14,510	30	17,008	17,527	17,257
233848	50–51 cm	14,640	35	17,157	17,744	17,435
233849	72–73 cm	21,330	60	24,883	25,475	25,157
233850	98–99 cm	30,300	140	34,064	34,664	34,366

3.5. Stable oxygen isotope and $CaCO_3$ stratigraphies and age model

In addition to ^{14}C, benthic (*Cibicidoides kullenbergi*) and planktic (*Globigerina bulloides*) $\delta^{18}O$ values were used to tune the age model of core TT1811-34GGC and provide the stratigraphy deeper in the core. The down-core variability in both $\delta^{18}O$ records are interpreted as primarily reflecting changes in global ice volume across the last glacial cycle, and agree well with global $\delta^{18}O$ stack of Lisiecki and Raymo (2005). The pattern of change in the $CaCO_3$ contents of TT1811-34GGC sediments is consistent with glacial-interglacial cycles in other sedimentary $CaCO_3$ records from the Southern Ocean and reflects decreases in biological productivity and $CaCO_3$ preservation during glacial intervals (Connell and Sikes, 1997). The benthic $\delta^{18}O$ and carbonate stratigraphy of core TT1811-34GGC are used to identify chronostratigraphic tie points with the LR04 benthic stack of Lisiecki and Raymo (2005). These tie-points form the basis of the age model of core TT1811-34GGC for MIS stages MIS 5 to 3, and as a supplement to radiocarbon analyses during the Holocene and late glacial period. A lack of *C. kullenbergi* between 230 and 242 cm necessitates the use of a planktic $\delta^{18}O$ tie point at 234 cm (82 ka, Fig. 2 and SOM Fig. 2). The $\delta^{18}O$ stratigraphy of core TT1811-34GGC indicates the base of the core dates to 118 ka (Fig. 3). Although sediments dating to the peak interglacial conditions of

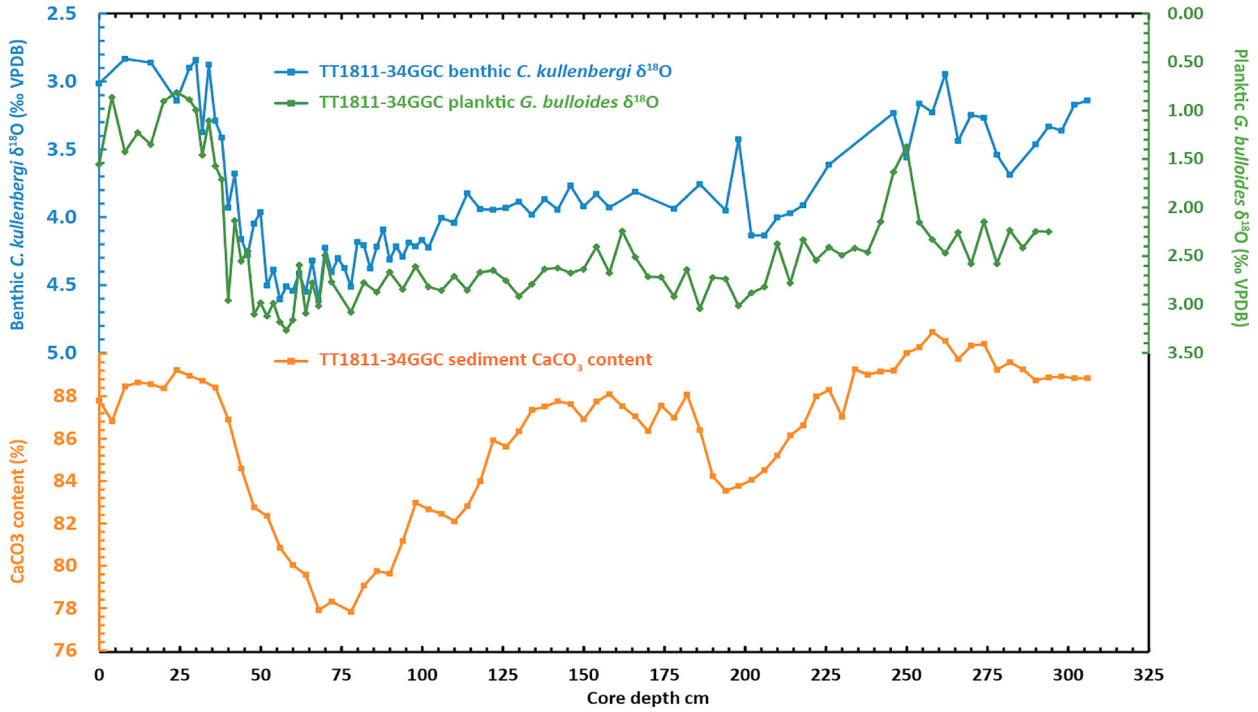

Fig. 2. Benthic *C. kullenbergi* (blue) and planktic G. *bulloides* (green) $\delta^{18}O$ alongside sedimentary $CaCO_3$ contents (orange) of core TT1811-34GGC.

MIS 5.5 were not recovered in core TT1811-34GGC, ε_{Nd} values of −8.0 to −8.8 during the later stages of MIS 5.5 (118–115 ka) are similar to those of the late Holocene (−8.6 at 2.55 ka).

4. Results

4.1. Neodymium isotopes

The ε_{Nd} record of TT1811-34GGC demonstrates pronounced glacial-interglacial variability, with generally more radiogenic (i.e. more positive) values throughout the last glacial period (MIS 4–2), and less radiogenic values (i.e. more negative) during MIS 5 and MIS 1 (Fig. 3). Although there are no measurements of modern seawater ε_{Nd} from LCDW close to our core site, our reconstructed late Holocene (2.55 ka) seawater ε_{Nd} of -8.6 ± 0.3 is in excellent agreement with modern CDW values of approximately −9.5 to −8.5 in the Atlantic and western Indian Southern Ocean and c. −8.5 in the western Pacific Southern Ocean (Bertram and Elderfield, 1993; Stichel et al., 2012; Basak et al., 2015). The peak interglacial of MIS 5.5 (approximately 123–129 ka) is not recorded in the sediments of TT1811-34GGC, however ε_{Nd} values of −8.8 to −8.0 at 115–118 ka are similar to late Holocene values. Radiogenic maxima of −6.9 (104.7 ka) and −7.5 (89 ka) during cool substages MIS 5.4 and MIS 5.2 are punctuated by less radiogenic values of −8.5 during warmer substages MIS 5.3 (96 ka) and MIS 5.1 (86.7 ka). At the MIS 5/4 transition (75–68 ka), there is a sharp shift of more than 2 epsilon units towards more radiogenic values followed by a gradual shift towards less radiogenic values during MIS 3. From MIS 3 into the LGM, there is a gradual increase – punctuated by more rapid millennial scale variability –, culminating in an LGM radiogenic peak of −6.0 at 22.6 ka. Across the glacial termination a shift towards less radiogenic values occurs, from −6.2 at 16.2 ka to −9.1 at 10.9 ka. Notably, the sharpest decrease in ε_{Nd} during the deglacial period occurs during the second half of deglaciation between 14.9 ka-10.9 ka (from −6.8 to −9.1), spanning and immediately following Antarctic Isotope Maximum 1 and the Antarctic Cold Reversal.

4.2. Sortable silt

Empirical relationships between flow speed and size sorting in marine sediment have been determined both by field calibration studies (McCave et al., 2017; Wu et al., 2019) and by laboratory flume tank experiments (Culp et al., 2020). Whilst the slope and intercept of such relationships evidentially varies between regions and sediment regimes, the general agreement between studies implies that in a given depositional environment, a linear scaling between $\overline{ss}$ and near-bottom flow speed occurs. However, the interpretation of paleoceanographic records is more complex if, for example, the size distribution and distance from the source of the terrigenous sediment varies over time. In the SE Indian Ocean, changes in sea level during glacial and cold intervals may indeed have modified the source regions of terrigenous sediment deposited in the deep-sea, by exposing shelf material and altering erosional patterns. At TT1811-34GGC, this may have manifested in increased sediment supply from the nearby volcanic islands Ile St Paul and Ile Amsterdam (labelled ISP in Fig. 1). In the absence of a dominant current-sorted signal, such a shift to a more proximal sediment source during glacial intervals would likely be reflected in coarser silt grain sizes, due to down-current fining (McCave and Hall 2006), and the coarser nature of these volcanic inputs. Instead, we see the inverse relationship, with cold intervals (and hence low sea level) associated with lower $\overline{ss}$ values, likely reflecting selective deposition by slower near-bottom flow. We therefore reason that the $\overline{ss}$ record presented here can be interpreted as reflecting variations in near-bottom flow speed (McCave et al., 2017).

The $\overline{ss}$ record of 34GGC is similar in structure to ε_{Nd} data, with higher values during interglacials and generally lower values during the last glacial (Fig. 3). This coupling between the $\overline{ss}$ and ε_{Nd} data suggest a similar circulation control on both proxies ($r^2 = 0.46$, Fig. 4). Following generally higher values during MIS 5.5, $\overline{ss}$ values

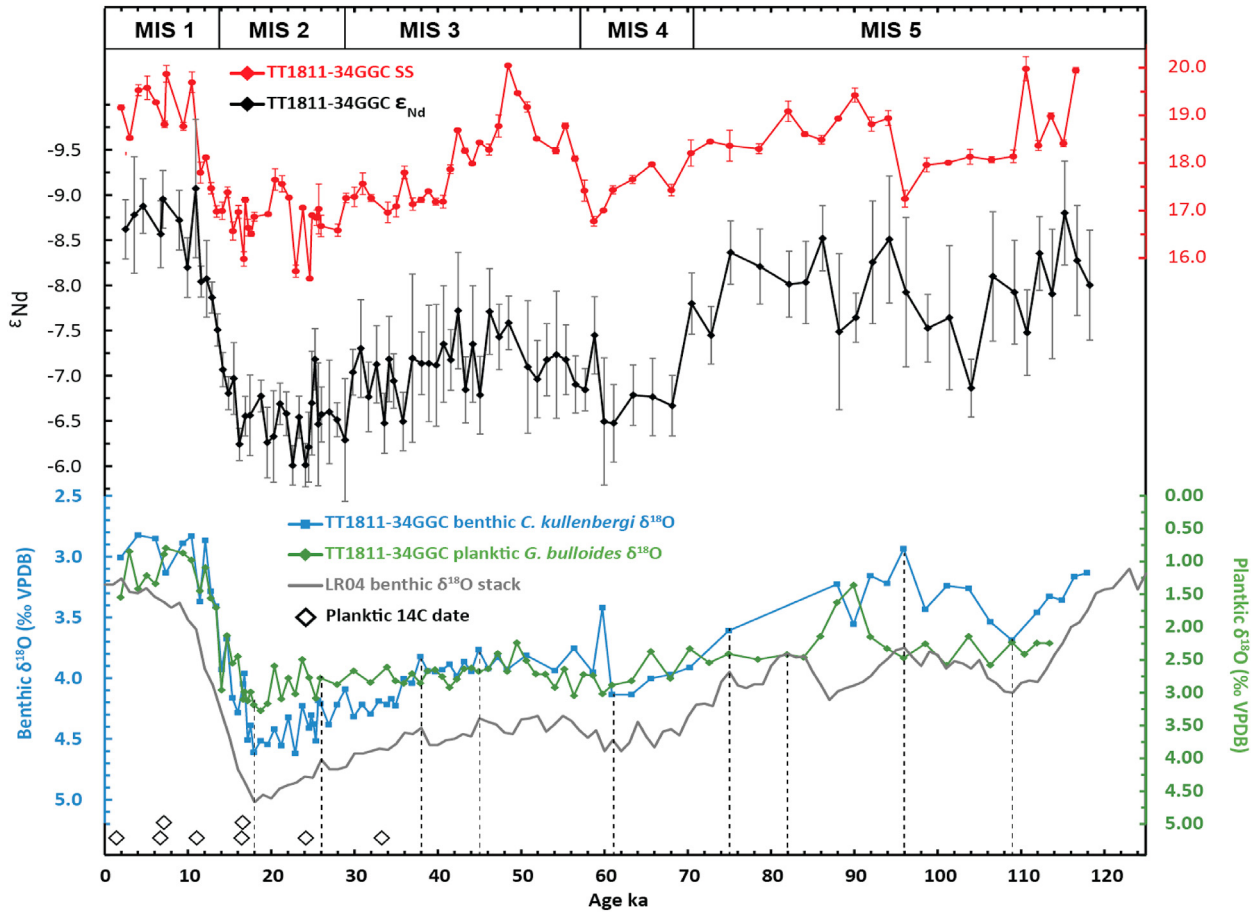

Fig. 3. The mean size of the sortable silt size fraction (ss, red) and Nd isotope record (ε_{Nd}, black) of core TT1811-34GGC plotted vs age. Benthic *C. kullenbergi* (blue) and planktic *G. bulloides* (green) $\delta^{18}O$ are also shown alongside the LR04 benthic $\delta^{18}O$ stack (grey, Lisiecki and Raymo 2005). The location of planktic radiocarbon dates used in creation of the age model are shown as black diamonds. The location of chronostratigraphic tie points between TT1811-34GGC and the LR04 stack are shown as dashed lines. Marine Isotope Stages (MIS) defined by Lisiecki and Raymo (2005) are shown at the top.

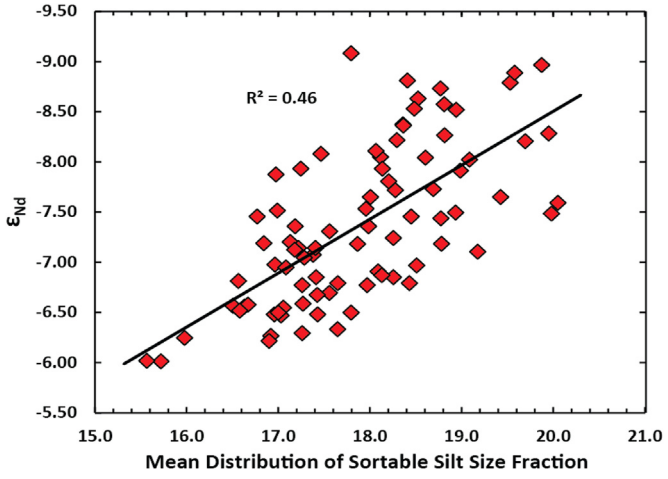

Fig. 4. A cross plot of Sortable Silt (ss) and ε_{Nd} values in core TT1811-34GGC demonstrates the coupling between changes in water mass sourcing and bottom water flow speeds during the last glacial cycle. Periods of reduced NCW mixing into the deep Southern Ocean (more radiogenic ε_{Nd}) coincide with reduced bottom water flow speeds (smaller ss).

decrease into MIS 5.4 and remain low throughout the first half MIS 5.3. There is a gradual decline in $\overline{ss}$ values from a maximum at 92.3 ka across the MIS 5/4 transition, with a minimum during the latter stages of MIS 4 at 58.7 ka. $\overline{ss}$ values during MIS 3 recover to similar levels as the early stages of MIS 5 and the Holocene, followed by a rapid two-step decline across 48.4–40.6 ka. This is followed by a more gradual decline towards the LGM – punctuated by millennial-scale variability similar to that of the ε_{Nd} record – culminating in a minimum at 22.6–23.8 ka. A slight increase in $\overline{ss}$ during the LGM peaks at 20.3 ka, followed by a decrease to a minimum at 16.2 ka. A rise in $\overline{ss}$ through the early stages of deglaciation between 16.2 and 14.8 ka occurs in tandem with changes in ε_{Nd}, while the bulk of the deglacial rise in $\overline{ss}$ (12.9–10.0 ka) overlaps with but appears to slightly lag the decrease in ε_{Nd}.

5. Discussion

The LGM in core TT1811-34GGC is notable for having the most radiogenic ε_{Nd} values and smallest $\overline{ss}$ grainsizes of the entire core. Together, shifts towards more radiogenic ε_{Nd} values and smaller $\overline{ss}$ grainsize argue for reduced current speeds accompanied by reduced entrainment of NCW into LCDW in the Indian sector of the Southern Ocean. This reduced NCW influence is observed throughout the last glacial cycle, particularly during MIS 2 and MIS 4, but also during the cool substages of the last interglacial, MIS 5.2 and 5.4. Reductions in bottom water flow speeds were most pronounced during MIS 2 and 4, and MIS 5.3 and MIS 5.4. Bottom water flow speeds during MIS 3 were generally higher than during MIS 2

and 4, and at times during the early stages of MIS 3 were similar to the Holocene despite the reduced influence of NCW in the deep Indian Ocean sector of the Southern Ocean (Fig. 3).

5.1. Deep Southern Ocean circulation across the last glacial period and Holocene

The spatial and temporal pattern of circulation changes within the Atlantic and Indian sectors of the Southern Ocean across the last glacial to late Holocene (MIS 4–1, 71–2 ka) is elucidated by comparing the new ε_{Nd} data of core TT1811-34GGC to the published records from the region (section 2.2) (Fig. 5). All records exhibit a similar magnitude of deglacial ε_{Nd} change (Fig. 5), reflecting a common circulation control on Southern Ocean seawater ε_{Nd} through the last glacial period and into the Holocene. Although sharing a similar structure to the other records, ε_{Nd} at the mid-depth ODP Site 1088 (2088 m. water depth), well positioned to monitor inflow from the Atlantic into the Southern Ocean, was bathed in waters with a higher proportion NCW (i.e. less radiogenic) than sites bathed in LCDW and modified CDW throughout the last glacial period (Fig. 5). This distinction in ε_{Nd} between sites suggests a more heterogenous Southern Ocean during the last glacial period, when density-driven stratification is believed to have limited mixing between water masses (McCave et al., 2008; Williams et al., 2019) and NCW entrainment within the Southern Ocean was supressed due to a shoaling of NCW (Sikes et al., 2017).

Our core, TT1811-34GGC, is located immediately east of the Kerguelen-Ile St. Paul Passage, through which a significant portion of deep-water flow within the ACC is routed via the bathymetric barriers imposed by the Kerguelen Plateau and Ile Amsterdam/Ile St. Paul (Fig. 1). Today TT1811-34GGC sits at the depth of the core of LCDW and records the ε_{Nd} composition of LCDW within the Indian sector of the Southern Ocean, that is down-stream NCW mixing into the deep Southern Ocean. During the last glacial period the ε_{Nd} records in the deepest cores (TN057-21/RC11-83 and SK129-CR2) exhibit millennial scale variability, shifting towards more radiogenic values suggesting reduced NCW advection into the deep Southern Ocean during Heinrich Stadials (Piotrowski et al, 2004, 2009), that are known to be periods of greatly reduced NCW production and diminished AMOC (Heinrich, 1988; Bohm et al., 2015). Heinrich Stadials in these cores are interspersed with periods of increased NCW influence at the two core sites, evidenced by these records shifting towards the less radiogenic values at shallower ODP Site 1088. Shifts towards less radiogenic ε_{Nd} values at site

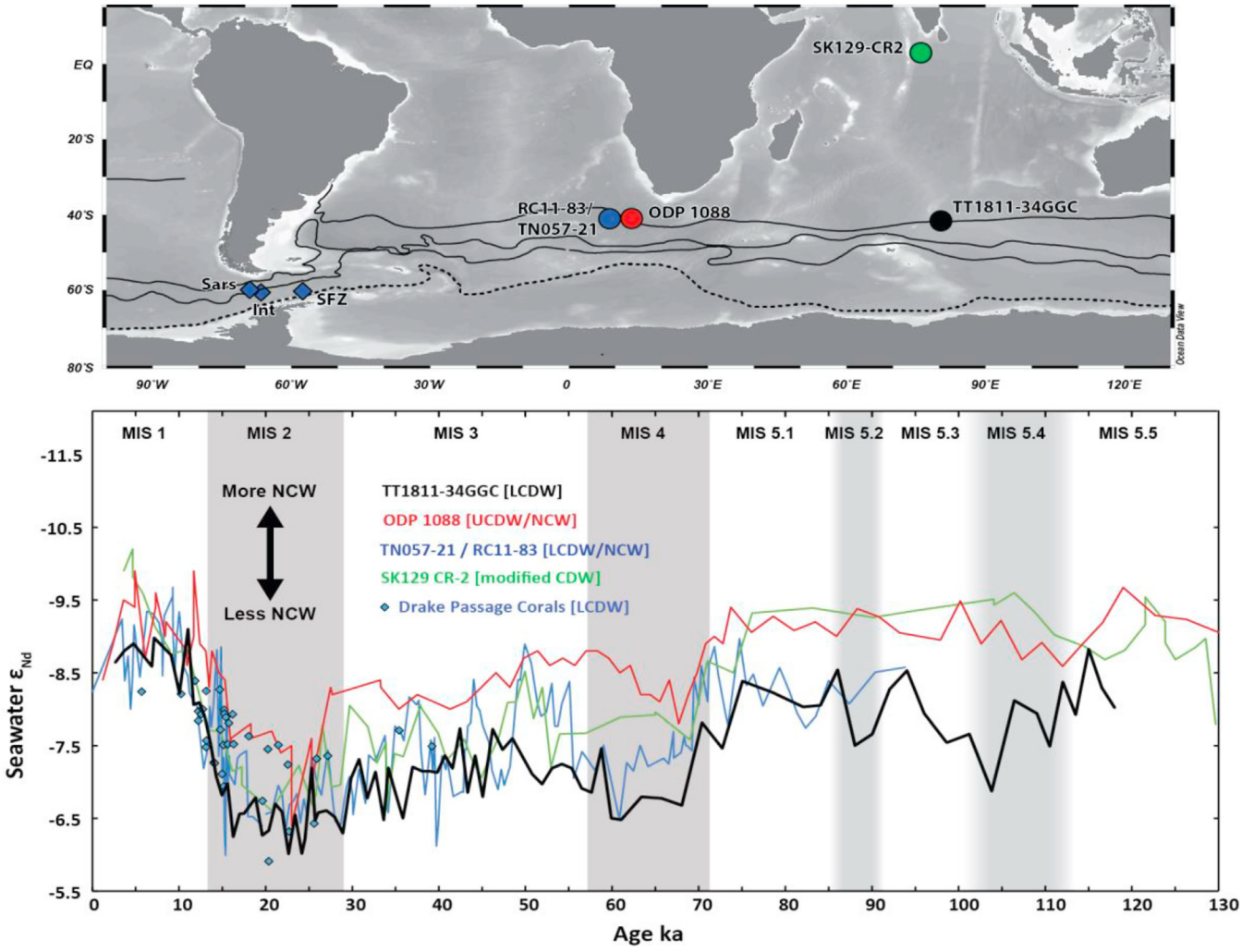

Fig. 5. A comparison of ε_{Nd} recorded at site TT1811-34GGC (this study), ODP Site 1088 (Hu et al., 2016), the composite records of RC11-83 and TN057-21 (Piotrowski et al., 2008, 2012), SK129-CR2 (Wilson et al., 2015), and coral samples located on the Sars seamount (Sars), Interim seamount (Int) and Shackleton Fracture Zone (SFZ) in Drake Passage (Wilson et al., 2020). From north to south black solid lines in the upper panel show the approximate locations of the Subtropical Front, Subantarctic Front and Antarctic Polar Front after Orsi et al. (1995). Dashed line is the southern boundary of the Antarctic Circumpolar Current (Orsi et al., 1995).

SK129-CR2 within the deep equatorial Indian Ocean suggest that during these periods of increased AMOC, some modified NCW was able to circulate around the southern tip of Africa and into the Indian basin, as occurs in the modern Southern Ocean. The ε_{Nd} record of TT1811-34GGC exhibits more muted variability throughout MIS 1–4, appearing less sensitive to millennial-scale variability in AMOC. ε_{Nd} at TT1811-34GGC maintains a more radiogenic ε_{Nd} signature than that of ODP Site 1088 throughout the last glacial period, with the exception of one data point during the LGM (Fig. 5).

The radiogenic ε_{Nd} data of core TT1811-34GGC indicate that the lower circulation cell was made up of a greater proportion of recirculated PDW throughout the last glacial period, not just during the LGM (Wilson et al., 2020; Yu et al., 2020). The offset in ε_{Nd} between our core T1811-34GGC and ODP Site 1088 suggests the inability of NCW from the South Atlantic to mix into the main body of LCDW across the entire last glacial period, even at times when AMOC may have been relatively strong (Bohm et al., 2015). This contrasts with the modern circulation regime, whereby NADW mixes into the deep Southern Ocean mainly within LCDW (Talley 2013). Today, LCDW serves as the precursor water mass for AABW, with NADW ultimately the main source of deep waters within the lower circulation cell (Talley 2013; Sloyan and Rintoul, 2001). During the LGM, shoaling of NCW waters to above 2500 m (Curry and Oppo 2005; Sikes et al., 2017) would have restricted their entry into the Southern Ocean (Sikes et al. 2017), leading to NCW being 'disconnected' from directly contributing to much of the deep ocean interior, with PDW effectively replacing NCW in the lower circulation cell (Wilson et al., 2020; Yu et al., 2020). Despite a greatly diminished contribution of NCW to the lower circulation cell, as evidenced by the more radiogenic ε_{Nd}, circumpolar waters within the Atlantic and Indian sectors of the Southern Ocean never reach the more radiogenic values of −2 to −4 that would represent a pure PDW source during the last glacial cycle. We therefore hypothesise that during the last glacial cycle deep waters sourced within the Atlantic basin still contributed to the lower circulation cell, albeit at a much smaller degree, i.e. likely via diffusive mixing within the ocean interior (e.g. de Lavirgne et al., 2017).

5.2. Coupled changes in Southern Ocean circulation and Antarctic climate

To assess the relationship between Southern Ocean circulation and Antarctic climate, we compare our ε_{Nd} and $\overline{ss}$ records with the $\delta^{18}O$ of ice ($\delta^{18}O_{ice}$) within the EPICA Dronning Maud Land (EDML) ice core, a proxy for Antarctic temperature (Fig. 6A–B; EPICA Community Members, 2006). ε_{Nd} in TT1811-34GGC closely tracks $\delta^{18}O_{ice}$ throughout the last 118 kyr. Cooler Antarctic temperatures coincide with reduced NCW within LCDW. To quantitatively assess the relationship between our Southern Ocean circulation record and Antarctic climate, we interpolated at 1.5 kyr and smoothed using a 3kyr low pass filter the $\delta^{18}O_{ice}$ record of EDML, the ε_{Nd} record of TT1811-34GGC, and the atmospheric CO_2 record from Antarctic ice cores (Fig. 6C). The filtered and smoothed ε_{Nd} record is strongly correlated with both the EDML $\delta^{18}O_{ice}$ ($r = 0.88$) and atmospheric CO_2 ($r = 0.87$). The relationship is weaker for $\overline{ss}$ and $\delta^{18}O_{ice}$ ($r = 0.67$) and atmospheric CO_2 ($r = 0.63$; neither shown in Fig. 6), indicating a moderate relationship between Antarctic climate and bottom water flow speeds. We note that smoothing of the records has little effect on the relationships: the un-smoothed 1.5 kyr interpolated ε_{Nd} record of TT1811-34 GC is still strongly correlated with climatic indices ($\delta^{18}O_{ice}$ $r = 0.86$; CO_2 $r = 0.85$).

The tight coupling between deep circulation at site TT1811-34GGC and Antarctic temperature throughout the last 118 kyr is evident and particularly notable throughout the early stages of glacial inception, during MIS 5.4–5.1 (Fig. 6A–C). We interpret the MIS 5.5 ε_{Nd} values of core TT1811-34GGC as reflecting a similar-to-modern circulation regime whereby unradiogenic NCW flowed into the Southern Ocean and mixed into LCDW at depth. Following this, during MIS 5.4 between 110.5 and 101.2 ka, NCW entrainment in LCDW was greatly reduced, with ε_{Nd} values of −6.9- to −8.1 recorded (average $\varepsilon_{Nd} = -7.6$). These MIS 5.4 ε_{Nd} values are only moderately higher than ε_{Nd} values during MIS 4, within the last glacial period (average $\varepsilon_{Nd} = -6.9$), with one data point at 104 ka ($\varepsilon_{Nd} = -6.9$) comparable to values during MIS 4. This apparent reduction in the proportion of NCW was accompanied by a reduction in bottom water flow speeds as indicated by smaller $\overline{ss}$ (Fig. 6A). These early circulation changes occurred while less radiogenic ε_{Nd} records at both the shallower ODP Site 1088 and the deeper equatorial SK129-CR2 suggested continued advection of NCW out of the Atlantic at intermediate depths into the Southern Ocean and to abyssal depths in the equatorial Indian Ocean, suggestive of a Holocene-like, stable AMOC (Fig. 5). The ε_{Nd} record of RC11-83/TN057-21 from the deep Atlantic sector of the Southern Ocean has radiogenic values similar to TT1811-34GGC during late MIS 5, suggesting a similar circulation control on ε_{Nd} at both sites. These deeper Southern Ocean records suggest that the mechanism linking changes in climate and circulation in LCDW waters (the depth of our core) during the early stages of glacial inception was rooted in the Southern Ocean, rather than changes in AMOC.

The reduction in bottom water flow speeds and proportion of NCW bathing core TT1811-34GGC during the transition from MIS 5.5–5.4 coincided with a critical period of global cooling marking the initiation of the last glacial cycle. This cooling was most pronounced at high latitudes (Kohfeld and Chase, 2017) and coincided with the first major expansion in continental ice of the last glacial cycle (Lisiecki and Raymo, 2005). During MIS 5.4, approximately 75% of the total decrease in the EDML $\delta^{18}O_{ice}$ between the last interglacial period and the LGM occurred, indicating a substantial cooling of the Antarctic continent (Fig. 6B). Notably this Antarctic cooling at approximately 118 ka, leads the initial drop in atmospheric CO_2 at this time by approximately 3ka (Fig. 6, EPICA Community Members, 2004). Antarctic cooling going into MIS 5.4 was also accompanied by an expansion in Southern Ocean sea-ice (Fig. 6D, Wolff et al., 2006). Increased sea-ice is consistent with the increased abundance of the diatom *F. curta*, (a proxy for winter sea-ice) within the Atlantic Polar Frontal Zone, which peaked during MIS 5.4 (Fig. 6E, Gersonde and Zielinski, 2000; Kohfeld and Chase, 2017). Early expansion in Antarctic sea-ice has been implicated as a driver in the first drop in atmospheric CO_2 across 115–100 ka by reducing the ability of upwelled deep water to outgas in the high latitude Southern Ocean (Kohfeld and Chase, 2017). This 'capping' of the surface ocean could have been achieved by a combination of ice acting as a physical barrier alongside seasonal melting of ice creating a freshwater stratification of the surface ocean (Stephens and Keeling, 2000). A shallow stratification of the surface ocean is consistent with an observed reduction in diatom-bound $\delta^{15}N$ at 113–108 ka (Studer et al., 2015), which provides evidence of more complete utilisation of available nutrients, and thus, a reduction in the supply of nutrients upwelled to the high latitude surface Southern Ocean (Fig. 6E, Studer et al., 2015). Although the reduction in NCW bathing core TT1811-34GGC across the MIS 5.5 to 5.4 transition coincides with cooling recorded in the EDML $\delta^{18}O_{ice}$ record, the radiogenic peak in ε_{Nd} during MIS 5.4 does not coincide with the local minima in $\delta^{18}O_{ice}$ at approximately 109 ka, which occurs during the northern hemisphere insolation minimum. Rather, the ε_{Nd} minimum in TT1811-34GGC occurs at 104 ka, instead coinciding with the southern hemisphere insolation minimum. The timing of this ε_{Nd} minimum further suggests a close link between circulation changes and the wider southern hemisphere – rather than northern hemisphere –

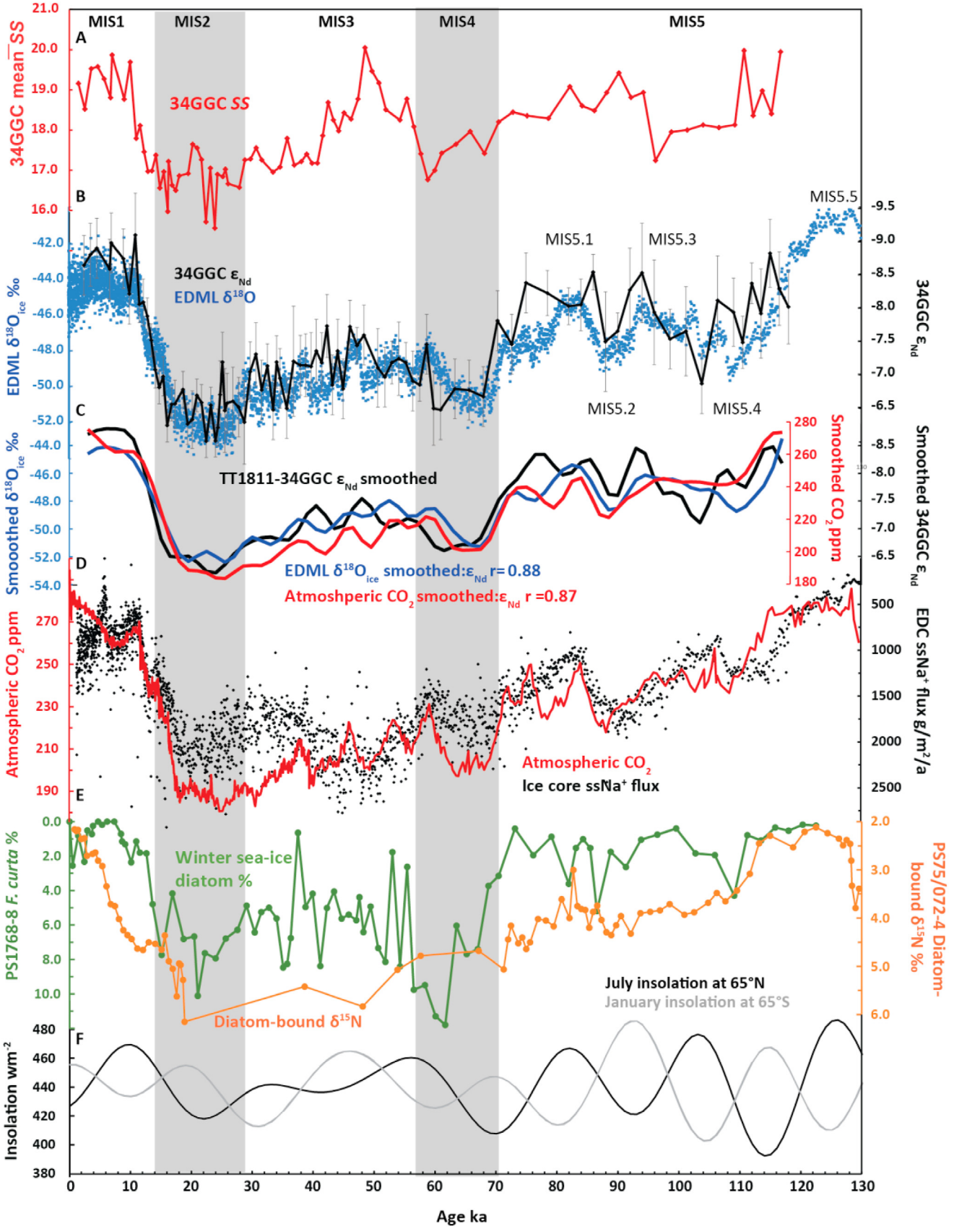

Fig. 6. A: The mean distribution of the sortable silt size fraction (SS) of core TT1811-34GGC. B: ε_{Nd} of core TT1811-34GGC (black) overlain on the $\delta^{18}O$ of ice in the EPICA Dronning Maud Land (EDML) ice core (blue, EPICA Community Members, 2006). C: Interpolated and smoothed ice core records of EDML $\delta^{18}O$, atmospheric CO_2 from Antarctic ice cores (EPICA Community Members 2004; EPICA Community Members, 2006), and ε_{Nd} from TT1811-34GGC. r values indicate the correlation coefficients of ice core climate proxies with the ε_{Nd}

climate, although we acknowledge that this offset may in part reflect uncertainty within the age model of TT1811-34GGC during MIS 5 (Fig. 6F).

5.3. Southern Ocean circulation changes during the early periods of glaciation

The ε_{Nd} record of core TT1811-34GGC demonstrates that there was substantial reduction of NCW at ~3200 m within the Indian sector of the Southern Ocean associated with the cooling of the Antarctic continental margin and expanded sea-ice during the transition from MIS 5.5 to MIS 5.4. We suggest that this reorganisation of deep circulation was a direct consequence of the cooling and capping of the Southern Ocean by sea ice, which led to changes in bottom water formation mechanisms along the continental margin.

Within the modern Southern Ocean, NADW is able to mix into LCDW by virtue of its elevated density compared to that of PDW and IDW, which both mix into UCDW (Speer et al., 2000; Talley 2013). We hypothesise that this density gradient was reversed across the MIS 5.5–5.4 transition, such that PDW became denser than NCW, hampering the ability of NCW to mix into the deep Southern Ocean at depths below PDW (Fig. 7). Today, the precursor waters of AABW are produced via a mixture of supercooling of LCDW beneath floating ice shelves and brine rejection during sea-ice formation (Orsi et al., 1999). We suggest that the expansion of sea-ice around Antarctica during the early stages of glacial inception increased the proportion of AABW produced via brine-rejection, increasing the salinity of AABW. It is also possible that cooling led to an expansion of grounded ice around Antarctica, reducing the production of AABW formed via cooling beneath ice shelves, also increasing the proportion of open water deep water formation beneath sea ice. AABW, along with LCDW, is the main source of PDW within the Pacific basin. We hypothesise that this saltier AABW exiting the Southern Ocean into the Pacific basin led to an increase in the salinity – and therefore density – of the deep Pacific Ocean, and therefore ultimately of PDW. In this scenario, NCW was still able to mix into the Southern Ocean during MIS 5.4, but at shallower depths than during MIS 5.5. NCW thereby replaced PDW as the key component in UCDW. PDW took the place of NCW in feeding LCDW and thus the lower global circulation cell (Fig. 7). The resulting increased density contrast between LCDW and UCDW would have reduced mixing between the two water masses and therefore explains the increased heterogeneity of ε_{Nd} records during MIS 5.4–5.1 (Fig. 5). This hypothesis is consistent with recent modelling work proposing past intervals of increased density-driven stratification within the deep ocean interior were directly tied to lower atmospheric temperatures in the high latitude Southern Ocean (Jansen 2017). Specifically, Jansen (2017) found that lower atmospheric temperatures led to increased buoyancy loss in surface waters around Antarctica primarily through increased brine rejection during sea-ice production, driving an increased density gradient between NCW-sourced and AABW-sourced water masses within the global ocean interior. It has also been proposed that during periods of Southern Ocean cooling and expanded sea ice, icebergs calved from the Weddell Sea region of Antarctica were able to propagate further north towards the Atlantic basin, where they melted and contributed to a freshening of the upper circulation cell within the Atlantic (Starr et al., 2021). Starr et al. (2021) suggest this would lead to a freshening of NCW during periods of Antarctic cooling, which would act to further amplify the density contrast between NCW and PDW. Via both a salinification of PDW and a freshening of NCW, Southern Ocean cooling and increased sea-ice during MIS 5.4 would thus have led to a larger density contrast between the upper and lower circulation cell, increased stratification of the ocean interior, and thus a disconnect between the upper and lower circulation cells.

ε_{Nd} data from core TT1811-34GGC indicate that the proportion of NCW mixing into LCDW scaled with Antarctic temperature throughout MIS 5.5 to MIS 5.1, consistent with the model results of Jansen (2017) (Fig. 6B). While ε_{Nd} values at core sites ODP 1088 in the mid-depth Atlantic Southern Ocean and SK129-CR2 in the deep equatorial Indian Ocean did shift slightly towards more radiogenic values during MIS 5.4, neither core show evidence for a shift towards the much more radiogenic values observed in core TT1811-34GGC at this time (Fig. 5). These less radiogenic values indicate that NCW was still entrained within the mid-depth Southern Ocean at this time and may also have been able to circulate around the southern tip of Africa into the deep low latitude Indian Ocean, as modified NADW does today. The proportion of NCW bathing those core sites decreased substantially across the MIS 5–4 transition approximately 71 ka, reflecting a reduction in NCW entering the Southern Ocean at all depths, possibly in response to a more northerly position of Southern Ocean fronts (Hu et al., 2016).

5.4. A circulation control on atmospheric CO_2 decline during glacial inception

Owing to the previous lack of proxy evidence for deep circulation changes (e.g. Oliver et al.,2010; Wilson et al., 2015), the initial drop in atmospheric CO_2 during MIS 5.4 has been attributed to the increased presence of sea-ice around Antarctica, reducing outgassing of CO_2 in the high latitude Southern Ocean (Kohfeld and Chase, 2017; Stephens and Keeling, 2000). However, the effects of increased sea ice and associated seasonal meltwater input to the surface ocean on carbon storage within the deep ocean interior remain poorly constrained, with models providing conflicting results (Köhler et al., 2010; Toggweiler et al., 2006). The new ε_{Nd} and $\overline{ss}$ data from core TT1811-34GGC provide evidence for a previously unrecognised role in deep ocean circulation changes in this initial CO_2 decline, in agreement with recent box model findings (O'Neill et al., 2019). This box model study utilised extensive paleo-proxy data to suggest that the initial decrease in atmospheric CO_2 across 115–108 ka resulted from a reduction in global overturning circulation, from ~28 Sv during MIS 5.5–~19 Sv during MIS 5.4 (O'Neill et al., 2019). Importantly, this reduction in overturning circulation occurring outside of the Atlantic basin and absent a change in AMOC (O'Neill et al., 2019). These model findings suggest the reason that evidence for major deep-water circulation changes during MIS 5.4 have remained so far undetected is the bias towards the Atlantic in currently available paleocirculation proxies spanning this interval (e.g. Oliver et al., 2010). The lack of change in circulation within the Atlantic at this time also explains the continued inflow of NCW into the Southern Ocean evident in ε_{Nd} records from the mid-depth Atlantic (ODP Site 1088) and deep equatorial Indian Ocean (SK129-CR2) (Fig. 5). Our new ε_{Nd} data demonstrate that this inflow of NCW occurred at the depth of UCDW, rather than LCDW.

The strong correlation of TT1811-34GGC ε_{Nd} with atmospheric CO_2 ($r = 0.87$) throughout the last 118 ka (Fig. 6C) suggests that

paleocirculation proxy. D: A composite record of Antarctic ice core atmospheric CO_2 records (red, EPICA Community Members, 2004) alongside a record of sea salt-derived sodium ion ($ssNa^+$) flux to the EPICA Dome C ice core, a proxy for sea ice extent (black, Wolff et al., 2006). E: Abundance of the winter sea ice diatom *F. curta* in the sediments of core PS1768-8 located in the region of the Polar Front of the Atlantic Southern Ocean (green, Gersonde and Zielinski, 2000) and total diatom-bound d15 N in sediments from core PS75/072-4 located south of the Polar Front (Orange, Studer et al., 2015). F: Insolation during July at 65°N and January at 65°S.

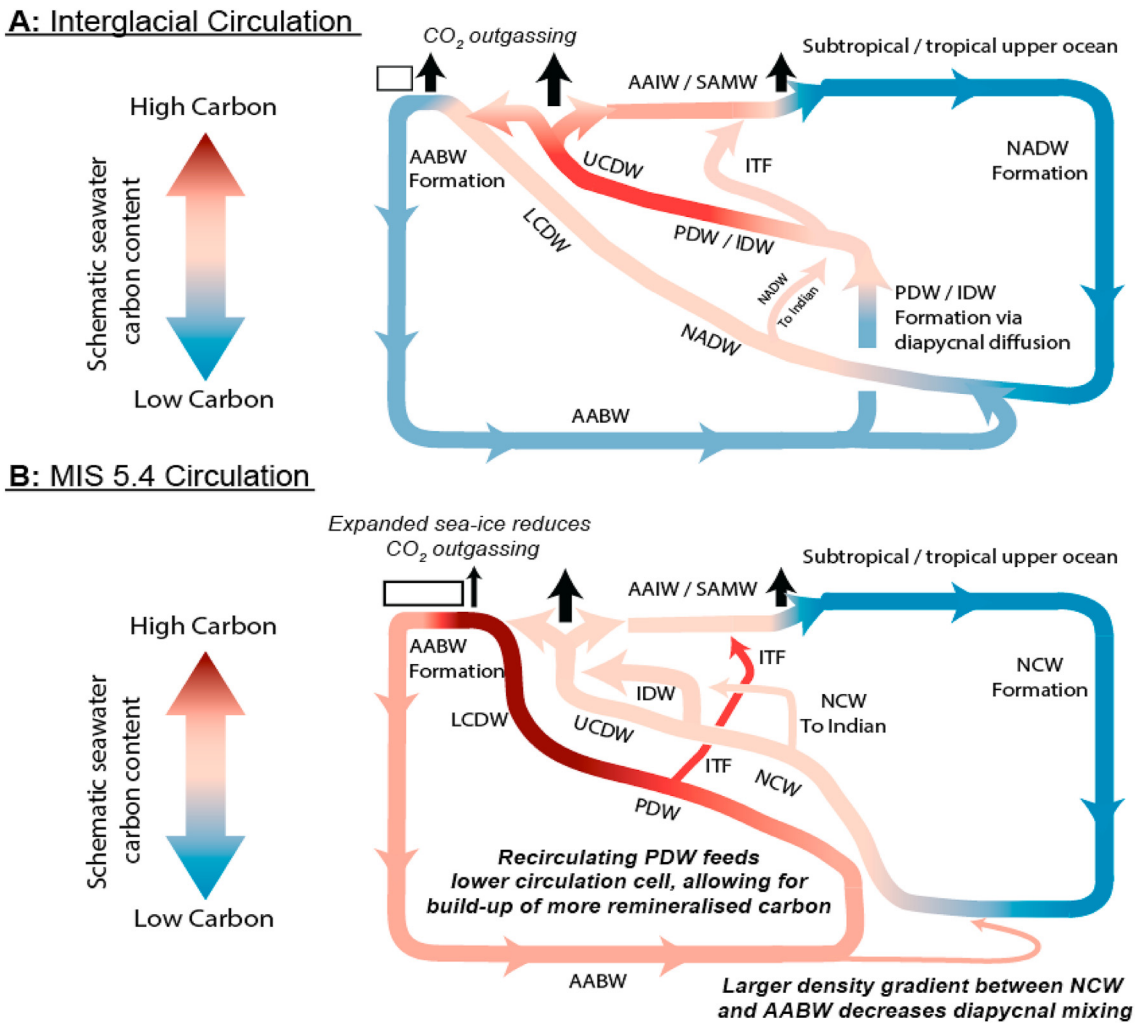

Fig. 7. A schematic global overturning circulation depicting idealized carbon content of water masses A: during interglacial periods and B: During the glacial inception of MIS 5.4. In the modern ocean NADW is denser than PDW, causing it to mix to depths below PDW within the Southern Ocean and form LCDW, which in turn upwells to form AABW. The lower circulation cell is thus sourced in NADW. During MIS 5.4, increased salinity of AABW due to expanded Southern Ocean sea-ice leads to an increase in PDW density such that it becomes denser than NCW. PDW thereby sinks below NCW within the Southern Ocean, becoming the main water mass sourcing LCDW, and thus AABW. Recirculating PDW thereby feeds the lower circulation cell, which becomes more isolated from AMOC. Together with reduced outgassing and a greater stratification of the ocean interior, this reorganisation of palaeocirculation leads to a greater storage of remineralised carbon within the deep circulation cell compared to interglacial periods. Circulation schematic after Talley (2013).

circulation changes within the deep Southern Ocean played a critical role in the lowering of atmospheric CO_2 during MIS 5.4. We propose that the reduced ability of NCW to mix into the deep Southern Ocean during MIS 5.4 was due to a reversal of the modern density gradient between Atlantic- and Pacific-sourced waters within the Southern Ocean. This density reversal between the two water masses led to a shoaling of NCW within the Southern Ocean, a reduction in the NCW component of LCDW, and PDW became the primary water mass feeding the lower circulation cell during MIS 5.4–5.1. (Fig. 7). This reorganisation of circulation would act to increase oceanic carbon storage via a "standing volume effect", whereby a smaller portion of the global ocean is ventilated by carbon-poor NCW at the expense of PDW, which is richer in remineralised carbon (Skinner, 2009) (Fig. 7). The more sluggish deep ocean circulation indicated by the $\overline{ss}$ record of TT1811-34GGC would also enable the build-up of a larger remineralised carbon pool within the deep ocean. The increased heterogeneity in Southern and Indian Ocean ε_{Nd} records suggests a reduced mixing within the Southern Ocean interior and thus a more stratified deep ocean, possibly owing to increased density contrasts between deep water masses sourced in the Atlantic and Pacific/Southern Oceans. This would slow overturning circulation and further reduce ventilation of this deep carbon pool (O'Neill et al., 2019). A role for ocean circulation changes in the atmospheric CO_2 decline during MIS 5.4 also helps explain the approximately 3 ka lag between the onset of Antarctic cooling (Fig. 6B) and increased sea-ice (Fig. 6D) compared to the fall in atmospheric CO_2 (Fig. 6D). The timescale of this lag is appropriate for a shift driven by global deep-water circulation. However, these mechanisms do not rule out a contribution to reduced atmospheric CO_2 during MIS 5.4 from reduced carbon outgassing within the high latitude Southern Ocean as suggested by Kohfeld and Chase(2017), which is also likely to have played a role.

6. Conclusions

This study presents combined ε_{Nd} and $\overline{ss}$ reconstructions of palaeocirculation from a sediment core retrieved from within the deep Indian sector of the Southern Ocean, TT1811-34GGCC. The sediments of this core span the last glacial cycle, from MIS 5.5 to

MIS 1. A reduction in the inflow of NCW to the deep Southern Ocean at the expense of PDW compared with the Holocene is inferred to have occurred throughout the last glacial period (MIS 2–4), based on shifts towards more radiogenic ε_{Nd} values during this interval. A concurrent reduction in bottom water flow speeds is inferred from smaller $\overline{ss}$ during MIS 2 and 4, although bottom water flow speeds were more similar to those of the Holocene during MIS 3. A strong correlation is observed between changes in the proportion of NCW mixing into LCDW and Antarctic climate – inferred from $\delta^{18}O$ of Antarctic ice – and atmospheric CO_2 concentrations. This tight coupling between palaeocirculation and palaeoclimate is observed throughout the last 118 ka, from MIS 5.5 through to the Holocene. Reductions in NCW mixing into the deep Southern Ocean are reconstructed for the first time to have occurred even during cool substages MIS 5.4 and 5.2. These changes during the early stages of the last glacial cycle occurred absent a change in AMOC, which was apparently as strong and stable as during the Holocene and the last interglacial period.

We attribute the reduction in NCW mixing into the deep Southern Ocean during the early stages of the last glacial cycle to a concurrent atmospheric cooling and expansion of sea-ice around Antarctic. We hypothesise that this expansion of sea-ice led to an increase in the formation of AABW via brine-reduction, increasing the salinity and therefore the density of AABW forming along the Antarctic continental margin. As AABW – along with LCDW, AAIW and SAMW – ultimately determine the properties of deep water within the Pacific basin, any increase in the density of AABW would inevitably have led to an increase in the density of PDW. We suggest that an increase in PDW density occurred in such a fashion during the transition from MIS 5.5 to 5.4, in doing so reversing the density gradient between NCW and PDW within the Southern Ocean. This reversal in density gradient prevented NCW from mixing into depths below PDW within the Southern Ocean. In this way PDW became the primary source of LCDW within the Southern Ocean during MIS 5.4–5.1, and thus recirculating PDW became the primary source of waters filling the deep ocean circulation 'cell', replacing NCW. Along with increased density stratification within the ocean interior and reduced outgassing of carbon from the high latitude Southern Ocean owing to increased sea-ice, this reorganisation of global ocean circulation acted to lower atmospheric CO_2 concentrations across the MIS 5.5 to 5.4 transition. This lowering of atmospheric CO_2 was a prerequisite for a sustained glaciation and thereby helped usher in the last glacial period.

Data availability

Datasets related to this article can be found at http://pangea.de.

Author statement

Thomas Williams: Conceptualization; Validation; Formal analysis; Investigation; Data curation; Writing – original draft; Writing – review & editing; Visualization; Project administration, Ellen Martin: Conceptualization; Validation; Writing – original draft; Writing – review & editing; Supervision; Project administration; Funding acquisition; Resources. Elisabeth Sikes: Conceptualization; Validation; Writing – original draft; Writing – review & editing; Supervision; Project administration; Funding acquisition; Resources. Aidan Starr: Conceptualization; Validation; Writing – original draft; Writing – review & editing; Data curation; Investigation, Natalie Umling: Conceptualization; Validation; Writing – original draft; Writing – review & editing; Investigation. Ryan Glaubke: Conceptualization; Validation; Writing – original draft; Writing – review & editing; Investigation

Declaration of competing interest

The authors declare that they have no known competing financial interests or personal relationships that could have appeared to influence the work reported in this paper.

Acknowledgements

We thank the officers, crew and shipboard scientists of R/V Thomas G. Thompson cruise TT1811. We thank Jamie Good for assistance in preparing sediment samples, Dr. Jason Curtis for analysing sedimentary percent $CaCO_3$ and benthic and planktic stable carbon and oxygen isotope analyses, and Dr. George Kamenov for assistance in Nd isotopic analyses. This study was made possible by the NSF OCE grant 1559080 and forms part of the Coring to Reconstruct Ocean Circulation and Carbon Dioxide Across 2 Seas (CROCCA-2S) project.

References

Anderson, R.F., Ali, S., Bradtmiller, L.I., Nielsen, S.H.H., Fleisher, M.Q., Anderson, B.E., Burckle, L.H., 2009. Wind-driven upwelling in the Southern Ocean and the deglacial rise in atmospheric CO_2. Science (80-.) 323, 1443–1448. https://doi.org/10.1126/science.1167441.

Ballarotta, M., Falahat, S., Brodeau, L., Döös, K., 2014. On the glacial and interglacial thermohaline circulation and the associated transports of heat and freshwater. Ocean Sci. 10, 907–921. https://doi.org/10.5194/os-10-907-2014.

Basak, C., Pahnke, K., Frank, M., Lamy, F., Gersonde, R., 2015. Neodymium isotopic characterization of Ross Sea bottom water and its advection through the southern south pacific. Earth Planet Sci. Lett. 419, 211–221. https://doi.org/10.1016/j.epsl.2015.03.011.

Bertram, C.J., Elderfield, H., 1993. The geochemical balance of the rare earth elements and neodymium isotopes in the oceans. Geochem. Cosmochim. Acta. https://doi.org/10.1016/0016-7037(93)90087-D.

Bohm, E., Lippold, J., Gutjahr, M., Frank, M., Blaser, P., Antz, B., Fohlmeister, J., Frank, N., Andersen, M.B., Deininger, M., 2015. Strong and deep Atlantic meridional overturning circulation during the last glacial cycle. Nature 517, 73–76. https://doi.org/10.1038/nature14059.

Ciais, P., Tagliabue, A., Cuntz, M., Bopp, L., Scholze, M., Hoffmann, G., Lourantou, A., Harrison, S.P., Prentice, I.C., Kelley, D.I., Koven, C., Piao, S.L., 2012. Large inert carbon pool in the terrestrial biosphere during the Last Glacial Maximum. Nat. Geosci. 5, 74–79. https://doi.org/10.1038/ngeo1324.

Connell, R.D., Sikes, E.L., 1997. Controls on late quaternary sedimentation of the south tasman rise. Aust. J. Earth Sci. 44, 667–675. https://doi.org/10.1080/08120099708728344.

Culp, J., Strom, K., Parent, A., Romans, B., 2020. Sorting of Fine-Grained Sediment by Currents: Testing the Sortable Silt Hypothesis with Laboratory Experiments. https://doi.org/10.31223/osf.io/xec2t.

Curry, W.B., Oppo, D.W., 2005. Glacial water mass geometry and the distribution of $\delta^{13}C$ of ΣCO_2 the western Atlantic Ocean. Paleoceanography 20, 1–12. https://doi.org/10.1029/2004PA001021.

De Lavergne, C., Madec, G., Roquet, F., Holmes, R.M., McDougall, T.J., 2017. Abyssal ocean overturning shaped by seafloor distribution. Nature 551, 181–186. https://doi.org/10.1038/nature24472.

Diekmann, B., Kuhn, G., Mackensen, A., Petschick, R., Futterer, D.K., Gersonde, R., Ruhlemann, C., Niebler, H.-S., 1999. Kaolinite and Chlorite as Tracers of Modern and Quaternary Deep Water Circulation.

EPICA Community Members, 2006. One-to-one coupling of glacial climate variability in Greenland and Antarctica. Nature 444, 195–198. https://doi.org/10.1038/nature05301.

EPICA Community Members, 2004. Eight glacial cycles from an Antarctic ice core. Nature 429, 623–628. https://doi.org/10.1038/nature02599.

Ferrari, R., Jansen, M.F., Adkins, J.F., Burke, A., Stewart, A.L., Thompson, A.F., 2014. Antarctic sea ice control on ocean circulation in present and glacial climates. Proc. Natl. Acad. Sci. Unit. States Am. 111, 8753–8758. https://doi.org/10.1073/pnas.1323922111.

Gebbie, G., Peterson, C.D., Lisiecki, L.E., Spero, H.J., 2015. Global-mean marine $\delta^{13}C$ and its uncertainty in a glacial state estimate. Quat. Sci. Rev. 125, 144–159. https://doi.org/10.1016/j.quascirev.2015.08.010.

Gersonde, R., Zielinski, U., 2000. The Reconstruction of Late Quaternary Antarctic Sea-Ice Distribution — the Use of Diatoms as a Proxy for Sea-Ice, vol. 162, pp. 263–286.

Gottschalk, J., Michel, E., Thole, L.M., Studer, A.S., Hasenfratz, A.P., Schmid, N., Butzin, M., Mazaud, A., Martinez-Garcia, A., Szidat, S., Jaccard, S.L., 2020. Glacial heterogeneity in Southern Ocean carbon storage abated by fast South Indian deglacial carbon release. Nat. Commun. 11, 6192. https://doi.org/10.1038/s41467-020-20034-1.

Heaton, T.J., Köhler, P., Butzin, M., Bard, E., Reimer, R.W., Austin, W.E.N., Bronk Ramsey, C., Grootes, P.M., Hughen, K.A., Kromer, B., Reimer, P.J., Adkins, J.,

Burke, A., Cook, M.S., Olsen, J., Skinner, L.C., 2020. Marine20—the marine radiocarbon age calibration curve (0–55,000 cal BP). Radiocarbon 62, 779–820. https://doi.org/10.1017/RDC.2020.68.
Heinrich, H., 1988. Origin and consequences of cyclic ice rafting in the Northeast Atlantic Ocean during the past 130,000 years. Quat. Res. 29, 142–152. https://doi.org/10.1016/0033-5894(88)90057-9.
Hodell, D.A., Venz, K.A., Charles, C.D., Ninnemann, U.S., 2003. Pleistocene vertical carbon isotope and carbonate gradients in the South Atlantic sector of the Southern Ocean. Geochem. Geophys. Geosyst. 4, 1–19. https://doi.org/10.1029/2002GC000367.
Hu, R., Piotrowski, A.M., Bostock, H.C., Crowhurst, S., Rennie, V., 2016. Variability of neodymium isotopes associated with planktonic foraminifera in the Pacific ocean during the Holocene and last glacial maximum. Earth Planet Sci. Lett. 447, 130–138. https://doi.org/10.1016/j.epsl.2016.05.011.
Huang, H., Gutjahr, M., Eisenhauer, A., Kuhn, G., 2020b. No detectable Weddell Sea antarctic bottom water export during the last and penultimate glacial maximum. Nat. Commun. 11, 1–10. https://doi.org/10.1038/s41467-020-14302-3.
Jansen, M.F., 2017. Glacial ocean circulation and stratification explained by reduced atmospheric temperature. Proc. Natl. Acad. Sci. Unit. States Am. 114, 45–50. https://doi.org/10.1073/pnas.1610438113.
Knox, F., McElroy, M.B., 1984. Changes in atmospheric CO_2: influence of the marine biota at high latitude. J. Geophys. Res. 89, 4629. https://doi.org/10.1029/JD089iD03p04629.
Kohfeld, K.E., Chase, Z., 2017. Temporal evolution of mechanisms controlling ocean carbon uptake during the last glacial cycle. Earth Planet Sci. Lett. 472, 206–215. https://doi.org/10.1016/j.epsl.2017.05.015.
Kohfeld, K.E., Ridgwell, a.J., 2009. Glacial-interglacial variability in atmospheric CO_2. Surf. Ocean - Low. Atmos. Process. 251–286. https://doi.org/10.1029/2008gm000845.
Köhler, P., Fischer, H., Schmitt, J., 2010. Atmospheric $\delta^{13}CO_2$ and its relation to pCO_2 and deep ocean $\delta^{13}C$ during the late Pleistocene. Paleoceanography 25, PA1213. https://doi.org/10.1029/2008PA001703.
Koutavas, A., 2018. Temperature correlations between the eastern equatorial Pacific and Antarctica over the past 230,000 years. Earth Planet Sci. Lett. 485, 43–54. https://doi.org/10.1016/j.epsl.2017.12.041.
Lambeck, K., Rouby, H., Purcell, A., Sun, Y., Sambridge, M., 2014. sea level and global ice volumes from the last glacial maximum to the Holocene. Proc. Natl. Acad. Sci. U.S.A. 111, 15296–15303. https://doi.org/10.1073/pnas.1411762111.
Lambelet, M., van de Flierdt, T., Crocket, K., Rehkämper, M., Kreissig, K., Coles, B., Rijkenberg, M.J.A., Gerringa, L.J.A., de Baar, H.J.W., Steinfeldt, R., 2016. Neodymium isotopic composition and concentration in the western North Atlantic Ocean: results from the GEOTRACES GA02 section. Geochem. Cosmochim. Acta 177, 1–29. https://doi.org/10.1016/j.gca.2015.12.019.
Lambert, F., Delmonte, B., Petit, J.R., Bigler, M., Kaufmann, P.R., Hutterli, M. a, Stocker, T.F., Ruth, U., Steffensen, J.P., Maggi, V., 2008. Dust-climate couplings over the past 800,000 years from the EPICA Dome C ice core. Nature 452, 616–619. https://doi.org/10.1038/nature06763.
Lisiecki, L.E., Raymo, M.E., 2005. A Pliocene-Pleistocene stack of 57 globally distributed benthic ^{18}O records. Paleoceanography 20, 1–17. https://doi.org/10.1029/2004PA001071.
Lumpkin, R., Speer, K., 2007. global ocean meridional overturning. J. Phys. Oceanogr. 37, 2550–2562. https://doi.org/10.1175/JPO3130.1.
Lund, D.C., Tessin, a C., Hoffman, J.L., Schmittner, A., 2015. Southwest Atlantic water mass evolution during the last deglaciation. Paleoceanography 30, 477–494. https://doi.org/10.1002/2014PA002657.
Lynch-stieglitz, J., Adkins, J.F., Curry, W.B., Dokken, T., Hall, I.R., Herguera, J.C., Hirschi, J.J., Ivanova, E.V., Kissel, C., Marchal, O., Marchitto, T.M., McCave, I.N., McManus, J.F., 2007. Atlantic Meridional Overturn. Glac. Max. 316, 66–69.
Marchitto, T.M., Curry, W.B., Oppo, D.W., 1998. Millennial-scale changes in North Atlantic circulation since the last glaciation. Nature 393, 557–561. https://doi.org/10.1038/31197.
Marcott, S.A., Bauska, T.K., Buizert, C., Steig, E.J., Rosen, J.L., Cuffey, K.M., Fudge, T.J., Severinghaus, J.P., Ahn, J., Kalk, M.L., McConnell, J.R., Sowers, T., Taylor, K.C., White, J.W.C., Brook, E.J., 2014. Centennial-scale changes in the global carbon cycle during the last deglaciation. Nature 514, 616–619. https://doi.org/10.1038/nature13799.
Martin, J.H., 1990. Glacial-interglacial CO_2 change: the iron hypothesis. Paleoceanography 5, 1–13. https://doi.org/10.1029/PA005i001p00001.
Martínez-Botí, M.A., Marino, G., Foster, G.L., Ziveri, P., Henehan, M.J., Rae, J.W.B., Mortyn, P.G., Vance, D., 2015. Boron isotope evidence for oceanic carbon dioxide leakage during the last deglaciation. Nature 518, 219–222. https://doi.org/10.1038/nature14155.
McCartney, M.S., Donohue, K.A., 2007. A cyclonic gyre in the Atlantic Australian Basin. Prog. Oceanogr. 75, 675–750.
McCave, I.N., Carter, L., Hall, I.R., 2008. Glacial–interglacial changes in water mass structure and flow in the SW Pacific Ocean. Quat. Sci. Rev. 27, 1886–1908. https://doi.org/10.1016/j.quascirev.2008.07.010.
McCave, I.N., Hall, I.R., 2006. Size sorting in marine muds: processes, pitfalls, and prospects for paleoflow-speed proxies. Geochem. Geophys. Geosyst. 7 https://doi.org/10.1029/2006GC001284.
McCave N, Ian, Manighetti, Barbara, Robinson G, S, 1995. Sortable silt and fine sediment size/composition slicing: Parameters for palaeocurrent speed and palaeoceanography. Paleoceanogr. Paleoclimatol. 10 (3), 593–610. https://doi.org/10.1029/94PA03039.
McCave, I.N., Thornalley, D.J.R., Hall, I.R., 2017. Relation of sortable silt grain-size to deep-sea current speeds: calibration of the 'Mud Current Meter. Deep-Sea Res. Part I Oceanogr. Res. Pap. 127, 1–12. https://doi.org/10.1016/j.dsr.2017.07.003.
Mccorkle, D.C., Heggie, D.T., 1998. Glacial and Holocene stable isotope distributions in the southeastern Indian Ocean. Paleocnography 13, 20–34.
Monnin, E., Indermühle, A., Dällenbach, A., Flückiger, J., Stauffer, B., Stocker, T.F., Raynaud, D., Barnola, J.M., 2001. Atmospheric CO_2 concentrations over the last glacial termination. Science (80-.) 291, 112–114. https://doi.org/10.1126/science.291.5501.112.
Noble, T.L., Piotrowski, A.M., McCave, I.N., 2013. Neodymium isotopic composition of intermediate and deep waters in the glacial southwest Pacific. Earth Planet Sci. Lett. 384, 27–36. https://doi.org/10.1016/j.epsl.2013.10.010.
O'Neill, C., Hogg, A.M., Ellwood, M., Opdyke, B., Eggins, S., 2019. Sequential changes in ocean circulation and biological export productivity during the last glacial cycle: a model-data study. Clim. Past Discuss 1–33. https://doi.org/10.5194/cp-2019-146.
Oliver, K., Hoogakker, B.A.A., Crowhurst, S., Henderson, G.M., Rickaby, R.E.M., Edwards, N.R., Elderfield, H., 2010. A synthesis of marine sediment core $\delta^{13}C$ data over the last 150 000 years. Clim. Past 6, 645–673. https://doi.org/10.5194/cp-6-645-2010.
Orsi, A.H., Johnson, G.C., Bullister, J.L., 1999. Circulation, mixing, and production of antarctic bottom water. Prog. Oceanogr. 43, 55–109. https://doi.org/10.1016/S0079-6611(99)00004-X.
Orsi, A.H., Whitworth, T., W, D.N., 1995. On the meridional extent and fronts of the Antarctic Circumpolar Current. Deep. Res. Part I Oceanogr. Res. Pap. 42.
Park, Y.H., Gambéroni, L., Charriaud, E., 1991. Frontal structure and transport of the antarctic circumpolar current in the South Indian Ocean sector, 40–80°E. Mar. Chem. 35, 45–62. https://doi.org/10.1016/S0304-4203(09)90007-X.
Paterne, M., Michel, E., Héros, V., 2019. Variability of marine 14C reservoir ages in the Southern Ocean highlighting circulation changes between 1910 and 1950. Earth Planet Sci. Lett. 511, 99–104. https://doi.org/10.1016/j.epsl.2019.01.029.
Piepgras, D., Wasserl, G., 1982. Isotopic composition of neodymiu in waters from the Drake passage. Science (80-.) 217, 207–214.
Piotrowski, A.M., Banakar, V.K., Scrivner, A.E., Elderfield, H., Galy, A., Dennis, A., 2009. Indian Ocean circulation and productivity during the last glacial cycle. Earth Planet Sci. Lett. 285, 179–189. https://doi.org/10.1016/j.epsl.2009.06.007.
Piotrowski M, Alexander, Galy, Albert, Joseph A L, Nicholl, Roberts, Natalie, Wilson J, David, Clegg A, Josephine, Yu, Jimin, 2012. Reconstructing deglacial North and South Atlantic deep water sourcing using foraminiferal Nd isotopes. Earth Planet. Sci. Lett. 357-358, 289–297. https://doi.org/10.1016/j.epsl.2012.09.036.
Piotrowski, A.M., Goldstein, S.L., Hemming, S.R., Fairbanks, R.G., 2004. Intensification and variability of ocean thermohaline circulation through the last deglaciation. Earth Planet Sci. Lett. 225, 205–220. https://doi.org/10.1016/j.epsl.2004.06.002.
Piotrowski M, Alexander, Goldstein L, Steven, Hemming R, Sidney, Fairbanks G, Richard, Zylberberg R, David, 2008. Oscillating glacial northern and southern deep water formation from combined neodymium and carbon isotopes. Earth Planet. Sci. Lett. 272 (1–2), 394–405. https://doi.org/10.1016/j.epsl.2008.05.011.
Reimer, P., Austin, W.E.N., Bard, E., Bayliss, A., Blackwell, P.G., Ramsey, C.B., Butzin, M., Cheng, H., Edwards, R.L., Friedrich, M., Grootes, P.M., Guilderson, T.P., Irka, H., Heaton, T., Hogg, A.G., Hughen, K.A., Kromer, B., Manning, S.W., Muscheler, R., Palmer, G., Pearson, C., van der Plicht, j., Reimer, R.W., Richards, D.A., Scott, E.M., Southon, J.R., Turney, C.S.M., Wacker, L., Adolphi, F., Buntgen, U., Capano, M., Fahrni, S.M., Fogtmann-Schulz, A., Friedrich, R., Kohler, P., Kudsk, S., Miyake, F., Ollsen, ., Reinig, F., Sakamoto, M., Sookdeo, A., Talamo, S., 2020. The IntCal20 northern hemisphere radiocarbon age calibration curve (0–55 cal kBP). Radiocarbon 62, 725–757. https://doi.org/10.1017/RDC.2020.41.
Roberts, N.L., Piotrowski, A.M., McManus, J.F., Keigwin, L.D., 2010. Synchronous deglacial overturning and water mass source changes. Science (80-.) 327, 75–78. https://doi.org/10.1126/science.1178068.
Sarmiento, J.L., Toggweiler, J.R., 1984. A new model for the role of the oceans in determining atmospheric pCO_2. Nature 308, 621–624. https://doi.org/10.1038/308621a0.
Shakun, J.D., Clark, P.U., He, F., Marcott, S.A., Mix, A.C., Liu, Z., Otto-Bliesner, B., Schmittner, A., Bard, E., 2012. Global warming preceded by increasing carbon dioxide concentrations during the last deglaciation. Nature 484, 49–54. https://doi.org/10.1038/nature10915.
Sigman, D.M., Hain, M.P., Haug, G.H., 2010. The polar ocean and glacial cycles in atmospheric CO_2 concentration. Nature 466, 47–55. https://doi.org/10.1038/nature09149.
Sikes, E.L., Allen, K.A., Lund, D.C., 2017. Enhanced $\delta^{13}C$ and $\delta^{18}O$ differences between the south atlantic and south pacific during the last glaciation: the deep gateway hypothesis. Paleoceanography 32, 1000–1017. https://doi.org/10.1002/2017PA003118.
Sikes, E.L., Samson, C.R., Guilderson, T.P., Howard, W.R., 2000. Old radio carbon agesin the southwest Pacific Ocean during the last glacial period and deglaciation. Nature 303, 555–559.
Skinner, L.C., 2009. Glacial-interglacial atmospheric CO_2 change: a possible "standing volume" effect on deep-ocean carbon sequestration. Clim. Past 5, 537–550. https://doi.org/10.5194/cp-5-537-2009.
Sloyan, B.M., Rintoul, S.R., 2001. The Southern Ocean limb of the global deep overturning circulation. J. Phys. Oceanogr. 31, 143–173, 10.1175/1520-

0485(2001)031<0143:TSOLOT>2.0.CO;2.
Snyder, C.W., 2016. Evolution of global temperature over the past two million years. Nature 538, 226–228. https://doi.org/10.1038/nature19798.
Speer, K., Rintoul, S.R., Sloyan, B., 2000. The diabatic deacon cell. J. Phys. Oceanogr. 30, 3212–3222, 10.1175/1520-0485(2000)030<3212:TDDC>2.0.CO;2.
Starr, Aidan, Hall R, Ian, Barker, Stephen, Rackow, Thomas, Zhang, Xu, Hemming R, Sydney, van der Lubbe, Jeroen, Knorr, Gregor, Berke A, Melissa, Bigg R, Grant, Cartagena-Sierra, Alejandra, Jiménez-Espejo J, Francisco, Gong, Xun, Gruetzner, Jens, Lathika, Nambiyathodi, LeVay J, Leah, Robinson S, Rebecca, Ziegler, Martin, Expedition 361 Science Party, 2021. Antarctic icebergs reorganize ocean circulation during Pleistocene glacials. Nature 589, 236–241. https://doi.org/10.1038/s41586-020-03094-7.
Stephens, B.B., Keeling, R.F., 2000. The influence of Antarctic sea ice on glacial-interglacial CO_2 variations. Nature 404, 171–174. https://doi.org/10.1038/35004556.
Stichel, T., Frank, M., Rickli, J., Haley, B.a., 2012. The hafnium and neodymium isotope composition of seawater in the Atlantic sector of the Southern Ocean. Earth Planet Sci. Lett. 317–318, 282–294. https://doi.org/10.1016/j.epsl.2011.11.025.
Studer, A.S., Sigman, D.M., Martínez-García, A., Benz, V., Winckler, G., Kuhn, G., Esper, O., Lamy, F., Jaccard, S.L., Wacker, L., Oleynik, S., Gersonde, R., Haug, G.H., 2015. Antarctic Zone nutrient conditions during the last two glacial cycles. Paleoceanography 30, 845–862. https://doi.org/10.1002/2014PA002745.
Stuiver, M., Reimer, P.J., Reimer, R.W., 2020. CALIB 8.2 [WWW program] at. http://calib.org. (Accessed 29 October 2020).
Tachikawa, K., Arsouze, T., Bayon, G., Bory, A., Colin, C., Dutay, J.-C., Frank, N., Giraud, X., Gourlan, A.T., Jeandel, C., Lacan, F., Meynadier, L., Montagna, P., Piotrowski, A.M., Plancherel, Y., Pucéat, E., Roy-Barman, M., Waelbroeck, C., 2017. The large-scale evolution of neodymium isotopic composition in the global modern and Holocene ocean revealed from seawater and archive data. Chem. Geol. https://doi.org/10.1016/j.chemgeo.2017.03.018.
Tachikawa, K., Piotrowski, A.M., Bayon, G., 2014. Neodymium associated with foraminiferal carbonate as a recorder of seawater isotopic signatures. Quat. Sci. Rev. https://doi.org/10.1016/j.quascirev.2013.12.027.
Talley, L.D., 2013. Closure of the Global Overturning Circulation through the Indian, Pacific and Southern Oceans: Schematics and Transports.
Tanaka, T., Togashi, S., Kamioka, H., Amakawa, H., Kagami, H., Hamamoto, T., Yuhara, M., Orihashi, Y., Yoneda, S., Shimizu, H., Kunimaru, T., Takahashi, K., Yanagi, T., Nakano, T., Fujimaki, H., Shinjo, R., Asahara, Y., Tanimizu, M., Dragusanu, C., 2000. JNdi-1: a neodymium isotopic reference in consistency with LaJolla neodymium. Chem. Geol. 168, 279–281. https://doi.org/10.1016/S0009-2541(00)00198-4.
Tierney, J.E., Zhu, J., King, J., Malevich, S.B., Hakim, G.J., Poulsen, C.J., 2020. Glacial cooling and climate sensitivity revisited. Nature 584, 569–573, 0.1038/s41586-020-2617-x.
Toggweiler, J.R., Russell, J.L., Carson, S.R., 2006. Midlatitude westerlies, atmospheric CO2, and climate change during the ice ages. Paleoceanography 21, 1–15. https://doi.org/10.1029/2005PA001154.
Umling, N.E., Oppo, D.W., Chen, P., Yu, J., Liu, Z., Yan, M., Gebbie, G., Lund, D.C., Pietro, K.R., Jin, Z.D., Huang, K.F., Costa, K.B., Toledo, F.A.L., 2019. Atlantic circulation and ice sheet influences on upper south Atlantic temperatures during the last deglaciation. Paleoceanogr. Paleoclimatol. 34, 990–1005. https://doi.org/10.1029/2019PA003558.
van de Flierdt, T. Van De, Griffiths, A.M., Lambelet, M., Little, S.H., Stichel, T., Wilson, D.J., 2016. Subject Areas : neodymium in the oceans : a global database , a regional comparison and implications for palaeoceanographic research. Philos. Trans. R. Soc. A 374. https://doi.org/10.1098/rsta.2015.0293.
Williams, T.J., Hillenbrand, C.D., Piotrowski, A.M., Allen, C.S., Frederichs, T., Smith, J.A., Ehrmann, W., Hodell, D.A., 2019. Paleocirculation and ventilation history of Southern Ocean sourced deep water masses during the last 800,000 years. Paleoceanogr. Paleoclimatol. 34, 833–852. https://doi.org/10.1029/2018PA003472.
Wilson, D.J., Piotrowski, A.M., Galy, A., Banakar, V.K., 2015. Interhemispheric controls on deep ocean circulation and carbon chemistry during the last two glacial cycles. Paleoceanography 30, 621–641. https://doi.org/10.1002/2014PA002707.
Wilson, D.J., Struve, T., van de Flierdt, T., Chen, T., Li, T., Burke, A., Robinson, L.F., 2020. Sea-ice control on deglacial lower cell circulation changes recorded by Drake Passage deep-sea corals. Earth Planet Sci. Lett. 544, 116405 https://doi.org/10.1016/j.epsl.2020.116405.
Wolff, E.W., Fischer, H., Fundel, F., Ruth, U., Twarloh, B., Littot, G.C., Mulvaney, R., Röthlisberger, R., de Angelis, M., Boutron, C.F., Hansson, M., Jonsell, U., Hutterli, M. a, Lambert, F., Kaufmann, P., Stauffer, B., Stocker, T.F., Steffensen, J.P., Bigler, M., Siggaard-Andersen, M.L., Udisti, R., Becagli, S., Castellano, E., Severi, M., Wagenbach, D., Barbante, C., Gabrielli, P., Gaspari, V., 2006. Southern Ocean sea-ice extent, productivity and iron flux over the past eight glacial cycles. Nature 440, 491–496. https://doi.org/10.1038/nature04614.
Wu, S., Kuhn, G., Diekmann, B., Lembke-Jene, L., Tiedemann, R., Zheng, X., Ehrhardt, S., Arz, H.W., Lamy, F., 2019. Surface sediment characteristics related to provenance and ocean circulation in the Drake Passage sector of the Southern Ocean. Deep-Sea Res. Part I Oceanogr. Res. Pap. 154, 103135 https://doi.org/10.1016/j.dsr.2019.103135.
Yokoyama, Y., Esat, T.M., Thompson, W.G., Thomas, A.L., Webster, J.M., Miyairi, Y., Sawada, C., Ze, T., Matsuzaki, H., Okuno, J., Fallon, S., Braga, J.-C., Humblet, M., Iryu, Y., Potts, D.C., Fujita, K., Suzuki, A., Kan, Hironobu, 2018. Rapid glaciation and a two-step sea level plunge into the Last Glacial Maximum. Nature 559, 603–607. https://doi.org/10.1038/s41586-018-0335-4.
Yu, J., Menviel, L., Jin, Z.D., Thornalley, D.J.R., Barker, S., Marino, G., Rohling, E.J., Cai, Y., Zhang, F., Wang, X., Dai, Y., Chen, P., Broecker, W.S., 2016. Sequestration of carbon in the deep Atlantic during the last glaciation. Nat. Geosci. 9, 319–324. https://doi.org/10.1038/ngeo2657.
Yu, J., Menviel, L., Jin, Z.D., Anderson, R.F., Jian, Z., Piotrowski, A.M., Ma, X., Rohling, E.J., Zhang, F., Marino, G., McManus, J.F., 2020. Last glacial atmospheric CO_2 decline due to widespread Pacific deep-water expansion. Nat. Geosci. 13, 628–633. https://doi.org/10.1038/s41561-020-0610-5.